An International Journal of Optimization and Control: Theories & Applications
ISSN: 2146-0957 eISSN: 2146-5703
Vol.16, No.5, pp.1993-2016 (2026)
https://doi.org/10.36922/IJOCTA026280152

RESEARCH ARTICLE

Neural network surrogate model analysis of couple stress squeeze film flow with slip velocity and piezo-viscous effects over rough circular plates

Mallesh Narayanareddy[1,2] and Vasanth Karegowdar Rajendrappa[1*]

[1]Department of Mathematics, NMAM Institute of Technology (NMAMIT), Nitte (deemed to be University), Udupi, Karnataka, India
[2]Department of Mathematics, Sahyadri College of Engineering and Management, Mangalore, Karnataka, India
mallesh.23pams103@student.nitte.edu.in, drvasanth@nitte.edu.in

ARTICLE INFO

Article History:
Received: July 8, 2026
Revised: August 24, 2026
Accepted: August 24, 2026
Published Online: September 14, 2026

Keywords:
Squeeze film
Viscosity variation
Couple stress fluid
Slip velocity
Roughness
Neural network surrogate model

ABSTRACT

Squeeze-film lubrication plays a crucial role in enhancing the performance, reliability, and service life of tribological components operating under high loads and varying lubrication conditions. This study investigates the squeeze-film lubrication characteristics of rough circular plates lubricated with a pressure-dependent viscous couple-stress fluid under slip velocity. A modified Reynolds equation is developed by incorporating Stokes' couple stress fluid theory, the Barus pressure–viscosity relationship, slip boundary conditions, and Christensen's stochastic surface roughness model. The governing equation is analyzed using a Neural network surrogate model (NNSM) to efficiently predict lubrication performance. The effects of the couple stress parameter, pressure–viscosity parameter, slip velocity, and surface roughness on dimensionless pressure, load-carrying capacity, and squeeze-film time are examined through analytical and numerical analyses. Results indicate that increasing the couple stress parameter enhanced pressure generation, load-carrying capacity, and squeeze-film duration, whereas increasing slip velocity generally reduced pressure and load-carrying capacity. Pressure-dependent viscosity significantly affects pressure distribution and load-supporting capability, while surface roughness produced distinct effects depending on its statistical orientation. The novelty of this work lies in integrating the NNSM with a lubrication model that simultaneously accounts for couple-stress fluid behavior, pressure-dependent viscosity, slip velocity, and surface roughness. The proposed approach provides an efficient method for predicting lubrication characteristics and offers valuable insights for the design and optimization of bearings, gears, seals, dampers, biomedical devices, and other tribological systems.

1. Introduction

Scientists, engineers, and industry have long recognized surface roughness as a significant topic. Surface texture is measured by how much the actual surface differs from its ideal shape. In bearings, this is referred to as roughness. A large variance indicates a rough surface, while a small variance indicates a smooth surface. The way mechanical systems operate is significantly impacted by roughness. Uneven surfaces can produce corrosion. As every bearing surface exhibits some degree of roughness, lubrication theory has recently attracted more interest for studying its effects. This study presents a novel neural network surrogate

*Corresponding Author

model (NNSM) to accurately and efficiently predict couple-stress squeeze-film lubrication with slip velocity, piezo-viscous effects, and stochastic surface roughness, enabling rapid design of advanced bearing and biomechanical systems.

Recently, using isothermal and isopiestic considerations, Barus[1] investigated the link between pressure and viscosity, providing the first understanding of how viscosity changes with external influences and laying the foundation for studying lubrication phenomena. Stokes[2] made a significant theoretical contribution by developing the theory of couple stresses in fluids and introducing microstructural effects, which served as the basis for non-Newtonian lubrication analysis. Bujurke and Jayaraman[3] examined non-Newtonian flow properties using the Stokes' couple-stress fluid in squeeze-film lubrication. Compared to Newtonian lubricants, the analysis shows that couple-stress lubricants greatly increase load-carrying capacity and squeeze-film duration, improving bearing performance and prolonging the service life of lubrication systems that resemble synovial joints. Cameron[4] laid the foundation for both hydrodynamic and boundary lubrication theories at about the same time by establishing systematic principles of lubrication. Kudenatti *et al.*[5] calculated magnetohydrodynamic (MHD) Reynolds equations for squeeze films. Ramanaiah[6] investigated the impact of couple-stress fluids on squeeze-film behavior, marking the beginning of research integrating non-Newtonian phenomena with squeeze-film lubrication. Elrod[7] incorporated Reynolds roughness into a generic laminar lubrication theory; Tripathi *et al.*[8] recently examined piezo-viscous squeeze films using analytical and coupled solution approaches. Hanumagowda *et al.*[9] used MHDs and couple-stress fluids to lubricate curved circular plates. Their work focused on the effects of magnetic fields, fluid microstructure, and curvature on squeeze film properties. For couple-stress fluid applications, lubrication theory was expanded to focus on film thickness, load capacity, and pressure distribution. Lin *et al.*[10] developed a modified lubrication formula for cylindrical squeeze films using the Stokes microcontinuum fluid model and the hydromagnetic flow model. The equation is illustrated with a parallel circular plate example. The findings show that hydromagnetic non-Newtonian lubricants enhance circular squeeze-film performance, particularly at higher magnetic fields and non-Newtonian parameters. While couple stress fluids, MHD effects, and piezoviscous lubrication have been thoroughly studied, little research has examined the combined effects of slip velocity, pressure-dependent viscosity, and surface roughness in circular squeeze film lubrication. Additionally, limited research has examined how radial and azimuthal roughness combine to affect the lubricating properties of couple stress fluids. Therefore, to enhance the prediction and optimization of squeeze film bearing performance, a thorough mathematical model that concurrently integrates these parameters is required.

Later, research began to link surface roughness to a major impact on hydrodynamic squeeze-film lubrication between contacting surfaces, changing key performance metrics such as response time, load-carrying capacity, and pressure distribution. Lin *et al.*[11,12] examined squeeze-film lubrication between parallel plates where the lubricant exhibits non-Newtonian couple-stress behavior and pressure-dependent viscosity. Compared to the traditional Newtonian iso-viscous scenario, the study examines how piezo-viscous effects and couple-stress factors affect load capacity and film performance. The study assesses improvements in squeeze-film properties under different viscosity–pressure parameters and film-thickness conditions using an approximate analytical solution with a minor perturbation method. Hanumagowda *et al.*[13] investigated a circular stepped plate with pressure-dependent viscosity and couple-stress squeeze-film lubrication. Tzeng and Saibel[14] initially emphasized the impact of surface roughness on lubrication performance; Christensen[15] developed stochastic models for hydrodynamic lubrication on rough surfaces. The impact of longitudinal random roughness upon a spherical surface & hemispherical bearing is examined using a stochastic lubrication theory with the modified Reynolds equation, proving that composite surface roughness negatively impacts bearing performance with spherical and circular squeeze film designs, as shown in previous studies by Prakash and Tonder,[16] Gupta and Deheri,[17] and Andharia *et al.*[18,19] These investigations have illustrated that the hydrodynamic squeeze-film lubrication system's performance is largely dependent on surface roughness. Using a stochastic method and the modified Reynolds equation, the effects of transverse as well as longitudinal random roughness for a squeeze film between a non-rotating spherical surface and a hemispherical bearing under steady load are examined in order to derive expressions for pressure, load-carrying capacity, as well as response time. According to the numerical and graphical data, composite surface roughness considerably lowers the bearing system's overall performance. Naduvinamani *et al.*[20] provided significant new information on sphere-plate systems, and the early

2000s further studied coupling stress and roughness effects in curved geometries. Over the following decade, advanced models incorporating non-Newtonian effects, external fields, and piezo-viscous dependency were developed. Naduvinamani et al.[21] further connected surface roughness and pressure-dependent viscosity, showing nonlinear impacts on squeeze performance. Hanumagowda et al.[22] and Fathima et al.[23] also examined circular plates and stepped geometries with pressure-dependent viscosity, roughness, and magnetic fields. Multiphysics couplings, such as ferrofluids and MHD, became a research focus in 2018. Hanumagowda et al.[24] investigated curved plates with couple stress and surface roughness, whereas Awati and Kengangutti[25] extended thermohydrodynamic analysis for journal bearings. As shown in the latest contributions of Byeon et al.,[26] which combine magnetohydrodynamics, viscosity fluctuation, and couple stress in squeeze films between flat and curved plates, the subject has evolved into a multiphysics domain. Kalavathi et al.[27] examined piezo-viscous squeeze films and porous bearings using analytical and coupled solution approaches. Surface roughness, magnetic field effects, and non-Newtonian lubricants greatly affect the effectiveness of squeeze film lubrication systems. The interplay of MHD flow, couple-stress fluids, and porous surfaces significantly influences pressure distribution and load-carrying capacity. As a result, studying these variables helps explain and improve lubrication performance in bearing systems, as shown by Hanumagowda et al.[28] Surface roughness, pressure-dependent viscosity, couple-stress fluids, and magnetic fields have all been extensively studied separately, but their combined impact with slip velocity in rough circular squeeze film lubrication is still mostly unknown. Therefore, a unified mathematical model is required to study the linked impacts of these parameters on squeeze film response time, load-carrying capacity, and pressure distribution.

Simultaneously, Patel and Deheri[29,30] examine how surface roughness and slip velocity affect the performance of a magnetic squeeze film based on the Jenkins model between curved, rough circular plates. The study uses the Christensen–Tonder stochastic roughness concept and the Beavers and Joseph slip model to investigate various surface geometries, including exponential, hyperbolic, and secant shapes. To find the pressure distribution and assess the bearing system's load-carrying capacity, the generalized Reynolds form equation is solved. The goal is to examine how magnetic effects, slip parameters, and roughness features affect squeeze film performance and to compare the Jenkins model's performance with the Neuringer–Rosensweig model. Sekar et al.[31] investigated velocity slip and viscosity fluctuations using porous stepped plates. Dass et al.[32] studied ferrofluid with slip-velocity effects. Vasanth et al.[33] and Mallesh et al.[34] also examined how couple stress, pressure-dependent viscosity, and slip velocity affect lubrication in the squeeze film between circular plates, including porous circular plates. The study investigated the lubricating system by considering key dimensionless elements such as pressure, load-carrying capacity, and squeeze-film duration. By showing how slip effects as well as pressure-induced viscosity variation dramatically change the couple-stress fluid's performance characteristics as compared with classical lubrication theory, their findings offered new insights into the mechanics of squeeze film behavior under complex fluid conditions. The combined impact of slip velocity, pressure-dependent viscosity, and stochastic surface roughness in rough circular squeeze film lubrication has not received enough attention, despite earlier research examining slip velocity in combination with couple stress fluids, pressure-dependent viscosity, porous media, and magnetic effects. To examine their combined impacts on pressure distribution, load-carrying capacity, and squeeze film reaction time under practical bearing conditions, a comprehensive model is needed.

Ang et al.[35] demonstrate the application of physics-informed neural networks (PINNs) as computationally efficient surrogate models for fluid dynamics by incorporating the concept of Navier–Stokes equations and boundary conditions directly into the neural network framework. Chen et al.[36] investigated continuous-depth neural network models based on ordinary differential equations, enabling memory-efficient, adaptive, and end-to-end trainable deep learning structures for dynamic and generative modeling tasks. Eivazi et al.[37] investigated PINNs to solve Reynolds-averaged Navier–Stokes equations for laminar and turbulent incompressible flows, achieving correct flow and Reynolds-stress predictions using only boundary values without explicit turbulence modeling. Jin et al.[38] developed PINN-based Navier–Stokes flow networks to accurately solve forward, inverse, and ill-posed incompressible flow problems, demonstrating flexible, data-efficient modeling for laminar and turbulent fluid dynamics. Jafari[39] examines research introducing a transport-embedded neural network that approximates complex fluid flow dynamics and overcomes false-minima errors in standard PINNs. Varun Kumar et al.[40] investigated a Laguerre polynomial-based PINN to analyze heat transfer in wavy permeable fins with ternary nanofluids, achieving accurate and computationally efficient thermal predictions under different physical parameters. Chandan *et al.*[41] investigated heat transfer in a concave permeable fin under local thermal non-equilibrium conditions using the clique polynomial method and PINNs, demonstrating accurate thermal predictions and efficient deep learning-based solutions for coupled heat transfer equations. Sanju *et al.*[42] examined the linear and weakly nonlinear stability of double-diffusive convection in a Navier–Stokes–Voigt fluid with chemical reaction and internal heat source effects, using the Runge–Kutta–Fehlberg method and PINNs to appropriately predict convection stability and mass–heat transfer characteristics. Chandan *et al.*[43] investigated the effect of radiation and temperature-dependent thermal conductivity on heat transfer in a radial fin using a PINN, supplying accurate and efficient thermal predictions with minimal training data. Varun Kumar *et al.*[44] analyzed hybrid nanofluid flow over a stretching cylinder under the effects of magnetic dipole, heat source/sink, and heterogeneous–homogeneous chemical reactions with the help of the Runge–Kutta–Fehlberg method and PINNs, illustrating accurate predictions of heat, mass, and flow characteristics. Varun Kumar *et al.*[45] investigated convective heat transfer in perforated rectangular fins with internal heat generation using a matrix-based Chelyshkov polynomial collocation approach, demonstrating improved heat transfer performance and accurate thermal predictions for different perforation parameters. Shah *et al.*[46] investigated a coupled dynamical system of materials recycling in chemostat systems using fractal fractional derivatives to capture the complex dynamics of recycling processes. The model is effectively analyzed, predicted, and validated using artificial deep neural networks (DNNs). This provides an accurate and intelligent framework for environmental and resource sustainability. Shah *et al.*[47] investigated the evolution of virulence using a fractional-order mathematical model integrated with DNNs to precisely capture memory-dependent disease dynamics. The proposed method provides reliable numerical analysis and improves understanding of complex epidemiological systems by combining fractional calculus, fixed point theory, and DNN-based prediction. Shah *et al.*[48] examined a fractional-order compartmental model of rotavirus transmission by integrating fractal fractional calculus with artificial DNNs to capture the complex dynamics of infectious disease spread. The proposed framework offers a precise and effective method for understanding epidemic dynamics and supporting disease management by combining mathematical analysis, numerical simulation, and DNN-based prediction. While DNNs and neural network surrogate models have been effectively applied to fractional mathematical models, fluid flow, and heat transfer, their application to coupling stress squeeze film lubrication with slip velocity, pressure-dependent viscosity, and stochastic surface roughness remains largely unexplored. To accurately predict lubrication features while reducing computational costs and maintaining high prediction accuracy, an NNSM-based surrogate framework must be developed.

This study examines the impact of slip velocity and viscous effects on fluid flow under the couple stress between rough circular plates. Expressions for the relationships between pressure, load, and time were derived, and numerical comparisons with traditional models were conducted. In light of previous research by Lin *et al.*,[12] Vasanth *et al.*,[33] and Mallesh *et al.*,[34] our study developed an NNSM that incorporates slip velocity, piezo-viscous effects, and stochastic surface roughness to forecast squeeze-film lubrication parameters quickly and accurately.

This work is innovative because it creates an NNSM that simultaneously incorporates slip velocity, piezo-viscous effects, and stochastic surface roughness to precisely forecast the lubrication features of couple stress squeeze film flow. The suggested model maintains good prediction accuracy for pressure distribution, load-carrying capacity, and squeeze film response time, while the proposed model significantly reduces computational time. The results offer a dependable design tool for sophisticated lubricating systems utilized in precision machinery, bearings, artificial synovial joints, and aerospace components.

2. Problem formulation in mathematics

Consider two axisymmetric rough circular plates separated by a thin fluid film. If the top plate moves toward the bottom plate at a squeezing velocity, the resulting radial flow in the fluid layer is governed by modified Reynolds equations that account for surface roughness. **Figure 1** illustrates the problem geometry.

Stokes is used to create a non-Newtonian micro-continuous fluid couple-stress model.[2] The following is the continuous equation that describes the lubricant flow in polar coordinates (r, y) (**Equations 1–3**):

$$\frac{\partial^2 u}{\partial y}^2 - \eta\frac{1}{\mu}\frac{\partial^4 u}{\partial y^4} = \frac{1}{\mu}\frac{\partial p}{\partial r} \tag{1}$$

$$\frac{\partial p}{\partial y} = 0 \tag{2}$$

$$\frac{\partial}{\partial r}(ru) = -r\frac{\partial v}{\partial y} \tag{3}$$

Equations 1–3 correspond to the boundary conditions. In this case, the fluid's velocity components along the coordinate directions are denoted by u and v. The fluid's viscosity is indicated by the parameter μ, the pressure is indicated by P, and the characteristic constant of the couple-stress fluid is represented by η. The velocities u and v at the upper and lower surfaces have the following boundary conditions **Equations 4 and 5**:

$$\text{At the surface below, } y=0, \quad u = \frac{\sqrt{k}}{\alpha}\left.\frac{\partial u}{\partial y}\right/_{y=0}, \quad \frac{\partial^2 u}{\partial y^2} = 0\ , v = 0 \tag{4}$$

$$\text{At the surface above, } y=h, u=0 \quad \frac{\partial^2 u}{\partial y^2} = 0, \quad v = -\frac{\partial h}{\partial t} \tag{5}$$

Equation 1 can be solved using **Equations 4 and 5**, resulting in **Equation 6**:

$$u = \{y^2 - h^2(\zeta_1 + \zeta_2 y)\}\frac{1}{2\mu}\frac{\partial p}{\partial r} + (h-y)\,\zeta_1$$
$$\frac{l}{\mu}\frac{\partial p}{\partial r} tanh\left(\frac{h}{2l}\right) + \frac{l^2}{\mu}\frac{\partial p}{\partial r}\left\{1 - \frac{cosh\left(\frac{2y-h}{2l}\right)}{cosh\left(\frac{h}{2l}\right)}\right\} \tag{6}$$

where $\zeta_1 = \frac{\sigma_1}{(h+\sigma_1)}$, $\zeta_2 = \frac{1}{(h+\sigma_1)}$

Using the continuity **Equation 1** to apply boundary conditions, we get **Equation 7**:

$$\frac{1}{r}\frac{\partial}{\partial r}\left(\left\{(1+3\zeta_1)h^3 - 12l^2h - 6h^2\zeta_1\ l\ tanh\left(\frac{h}{2}l\right) + 24\ l^3 tanh\left(\frac{h}{2l}\right)\right\}\frac{r}{\mu}\frac{\partial p}{\partial r}\right) = -12\frac{\partial h}{\partial t} \tag{7}$$

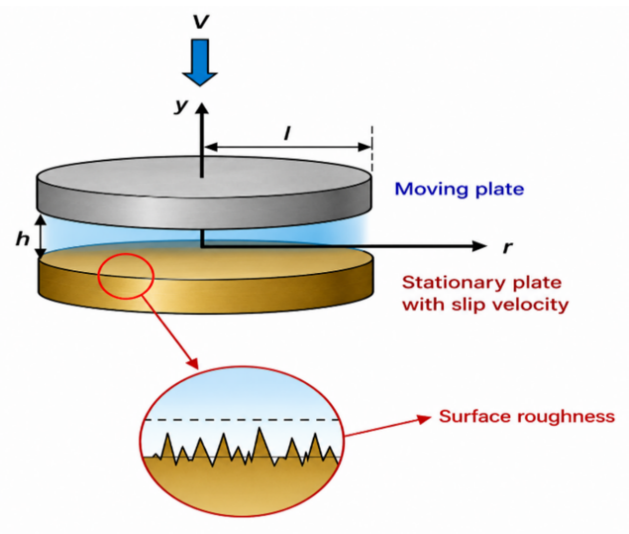

Figure 1. Geometry and model of rough circular plates with slip velocity

The following is the outcome of Barus[1] investigation into the relationship between viscosity and pressure (**Equation 8**):

$$\mu = \mu_0 e^{\alpha} p \tag{8}$$

when **Equation 8** is substituted into **Equation 7**, the result is a modified version of the Reynolds equation. This version accounts for pressure-dependent velocity on the circular plates and considers lubrication by a non-Newtonian fluid (**Equation 9**):

$$\frac{\partial}{\partial r}\left[f\left(h,\ m,\sigma,\alpha,p\right)r\frac{\partial p}{\partial r}\right] = -12r\mu_0\frac{\partial \mathrm{h}}{\partial t} \tag{9}$$

$$f\left(h,m,\sigma,\alpha,p\right) = (1+3\zeta_1)h^3e^{-\alpha p} - 12hm^2e^{-2\alpha p} - 6h^2$$
$$\zeta_1 m e^{\frac{-3\alpha p}{2}} tanh\left(\frac{he^{\frac{\alpha p}{2}}}{2m}\right) + 24m^3e^{\frac{-5\alpha p}{2}} tanh\left(\frac{he^{\frac{\alpha p}{2}}}{2m}\right)$$

$l = \left(\frac{\eta}{\mu}\right)^{\frac{1}{2}} = me^{\frac{-\alpha p}{2}}$, is the couple stress parameter.

The assumption is that the fluid film thickness consists of two components to numerically model surface roughness. $H_i = \mathrm{h}_i + \mathrm{h}_s(r,\theta,\xi)$.

The stochastic thickness h_s of the film's probability density function can be stated as $f(\mathrm{h}_s)$. Using the modified Reynolds **Equation 9** and its stochastic average with regard to $f(\mathrm{h}_s)$ (**Equations 10 and 11**):

$$\frac{1}{r}\frac{\partial}{\partial r}\left[E\left(f\left(h,m,\sigma,\alpha,p\right)\right)r\frac{\partial E(p)}{\partial r}\right] = -12\mu_0\frac{\partial \mathrm{h}}{\partial t} \tag{10}$$

$$\text{where } E(*) = \int_{-\infty}^{\infty}(*)f(h_s)dh_s \tag{11}$$

The roughness profile heights can be described using a Gaussian distribution up to at least three standard deviations for most lubricating surfaces. The function governing the roughness distribution is expected to have the following form, per Christensen[15] (**Equation 12**):

$$\mathrm{f}(\mathrm{h_s}) = \begin{cases} \frac{35}{32c^7}(c^2 - h_s^2)^3, & -c < h_s < c \\ 0, & \text{otherwise} \end{cases} \tag{12}$$

where, $c = 3\overline{\sigma}$ and $\overline{\sigma}$ be the standard deviation.

One-dimensional roughness patterns in both azimuthal and radial directions were investigated using Christensen's stochastic theory on lubricated rough surfaces.

2.1. Radial roughness

The thickness of the film is determined by one-dimensional radial roughness variations characterized by long, narrow ridges as well as valleys that radiate from the origin (z = 0, r = 0), creating a star-shaped pattern (**Equation 13**):

$$H_i = \mathrm{h}_i + \mathrm{h}_s(\theta, \xi) \tag{13}$$

2.2. Azimuthal roughness

The bearing surface's one-dimensional azimuthal roughness pattern is composed of valleys and long, thin ridges that run in the direction of θ. (On a flat plate, these are concentric circular ridges as well as valleys on $z = 0$, $r = 0$). The film thickness in this instance takes on the form $H_i = \mathrm{h}_i + \mathrm{h}_s(r, \xi)$.

The mean modified Reynolds equation from **Equation 10** is shown in **Equation 14**:

$$\frac{1}{r}\frac{\partial}{\partial r}\left\{\frac{1}{E\left(\frac{1}{f}\left(h, m, \sigma, \alpha, p\right)\right)} r \frac{\partial E\left(p\right)}{\partial r}\right\} = -12\mu_0 \frac{d\mathrm{h}}{dt} \tag{14}$$

From **Equations 10 and 14**, we get **Equation 15**:

$$\frac{1}{r}\frac{\partial}{\partial r}\left[g_i(h, m, \sigma, \alpha, p) r \frac{\partial E\left(p\right)}{\partial r}\right] = -12\mu_0 \frac{d\mathrm{h}}{dt} \tag{15}$$

where $g_i(h, m, \sigma, \alpha, p) = \begin{cases} E\left\{f(h, m, \sigma, \alpha, p)\right\} & \textit{for radial roughness} \\ \left[E\left\{1/f(h, m, \sigma, \alpha, p)\right\}\right]^{-1} & \textit{for azimuthal roughness} \end{cases}$

Now, $f\left(h, m, \sigma, \alpha, p\right) = (1 + 3\zeta_1)\mathrm{h}^3 e^{-\alpha p} - 12\mathrm{h}m^2 e^{-2\alpha p} - 6\mathrm{h}^2\zeta_1 m e^{\frac{-3\alpha p}{2}} \tanh\left(\frac{he^{\frac{\alpha p}{2}}}{2m}\right) + 24m^3 e^{\frac{-5\alpha p}{2}} \tanh\left(\frac{he^{\frac{\alpha p}{2}}}{2m}\right)$. Using the relevant dimensionless parameters, we obtain $r^* = \frac{r}{R}, l^* = \frac{m}{\mathrm{h}_{m0}}, \mathrm{h}^* = \frac{\mathrm{h}}{\mathrm{h}_{m0}}, \mathrm{h}^*_m = \frac{\mathrm{h}_m}{\mathrm{h}_{m0}}, \sigma = \frac{\sigma_1}{\mathrm{h}_{m0}}, P = \frac{p\mathrm{h}_{m0}{}^3}{\mu_0 R^2 \frac{\partial \mathrm{h}}{\partial t}}, G = \frac{\alpha\mu_0 R^2 \frac{\partial \mathrm{h}}{\partial t}}{\mathrm{h}_{m0}{}^3}$. This is the modified Reynolds equation in its dimensionless form (**Equations 16 and 17**):

$$\frac{\partial}{\partial r^*}\frac{1}{r^*}\frac{\partial}{\partial r^*}\left[g\left(\mathrm{h}^*, l^*, \sigma^*, G, P\right) r^* \frac{\partial p}{\partial r^*}\right] = -12 \tag{16}$$

where $g^*(h^*, l^*, \sigma^*, G, P) = \begin{cases} E\left\{f^*\left(\mathrm{h}^*, l^*, \sigma^*, G, P\right)\right\} & \textit{for radial roughness} \\ \left[E\left\{1/f^*\left(\mathrm{h}^*, l^*, \sigma^*, G, P\right)\right\}\right]^{-1} & \textit{for azimuthal roughness} \end{cases}$

$$\begin{aligned} f^*\left(h^*, l^*, \sigma^*, G, P\right) &= \left(1 + 3\zeta_1^*\right)\mathrm{h}^{*3} e^{-GP} - 12 \\ &\mathrm{h}^* l^{*2} e^{-2GP} - 6\zeta_1^* h^{*2} l^* e^{-1.5GP} \tanh\left(\frac{\mathrm{h}^* e^{0.5GP}}{2l^*}\right) \\ &+ 24 l^{*3} e^{-2,5GP} \tanh\left(\frac{\mathrm{h}^* e^{0.5GP}}{2l^*}\right) \end{aligned} \tag{17}$$

Using the perturbation technique, the viscosity parameter varies as $0 \leq G \leq 1$. The nondimensional pressure expression is shown in **Equation 18**:

$$P^* = P_0^* + GP_1^* \tag{18}$$

The pressure equations, P_0^* and P_1^*, are obtained by substituting **Equation 17** into Reynolds **Equation 15** and utilizing Maclaurin's series while ignoring the terms of G's second and higher order (**Equations 19 and 20**):

$$\frac{\partial}{\partial r^*}\left[r^* \frac{\partial P_0^*}{\partial r^*}\right] = -\frac{12r^*}{F_0\left(h^*, l^*, \sigma^*\right)} \tag{19}$$

$$\begin{aligned} \frac{\partial}{\partial r^*}\left[r^* \frac{\partial P_1^*}{\partial r^*}\right] &= -\frac{F_1\left(h^*, l^*, \sigma^*\right)}{F_0\left(h^*, l^*, \sigma^*\right)} \\ \frac{\partial}{\partial r^*}&\left[r^* P_0^* \frac{\partial P_0^*}{\partial r^*}\right] \end{aligned} \tag{20}$$

where (**Equations 21 and 22**):

$$\begin{aligned} F_0\left(h^*, l^*, \sigma^*\right) &= \left(1 + 3\zeta_1^*\right)\mathrm{h}^{*3} - 12h^* l^{*2} \\ &+ 6\left(4l^{*3} - \zeta_1^* \mathrm{h}^{*2} l^*\right)\tanh\left(\frac{\mathrm{h}^*}{2l^*}\right) \end{aligned} \tag{21}$$

$$\begin{aligned} F_1\left(h^*, l^*, \sigma^*\right) &= -\left(1 + 3\zeta_1^*\right) h^{*3} + 24\mathrm{h}^* l^{*2} \\ &+ 3\left(3\zeta_1^* \mathrm{h}^{*2} l^* - \ 20l^{*3}\right)\tanh\left(\frac{\mathrm{h}^*}{2l^*}\right) \\ &+ 1.5\left(4l^{*2}\mathrm{h}^* - \zeta_1^* \mathrm{h}^{*3}\right) sech^2\left\{\frac{\mathrm{h}^*}{2l^*}\right\} \end{aligned} \tag{22}$$

The solution for P_0^* and P_1^* is found from the solution of **Equations 19 and 20** as **Equations 23 and 24**:

$$P_0^* = -\frac{3\left(r^{*2} - 1\right)}{F_0\left(h^*, l^*, \sigma^*\right)} \tag{23}$$

$$P_1^* = -\frac{F_1\left(h^*, l^*, \sigma^*\right)}{\left[F_0\left(\mathrm{h}^*, l^*, \sigma^*\right)\right]^3}\left[\frac{9}{2}\left(r^{*2} - 1\right)^2\right] \tag{24}$$

By substituting **Equations 23 and 24** into **Equation 18**, we get the nondimensional pressure (**Equation 26**):

$$\begin{aligned} \mathrm{P} = &\left[-\frac{3(r^{*2} - 1)}{F_0\left(h^*, l^*, \sigma^*, C\right)}\right] \\ &- \mathrm{G}\left[\frac{9}{2}\frac{F_1\left(h^*, l^*, \sigma^*, C\right)}{\left[F_0\left(h^*, l^*, \sigma^*, C\right)\right]^3}\left(r^{*2} - 1\right)^2\right] \end{aligned} \tag{25}$$

The load-carrying capacity W^* is calculated using **Equation 26**:

$$W^* = 2\pi \int_0^1 P^* r^* dr \tag{26}$$

Following integration, the squeeze film's dimensionless load-bearing capacity can be written as **Equation 27**:

$$W^* = \frac{3\pi}{2}\left[\frac{1}{F_0\left(h^*, l^*, \sigma^*, C\right)} - G\left[\frac{F_1\left(h^*, l^*, \sigma^*, C\right)}{\left[F_0\left(h^*, l^*, \sigma^*, C\right)\right]^3}\right]\right] \tag{27}$$

For the constant load W^*, by analyzing **Equation 27**, the squeeze film duration T can be found using **Equation 28**:

$$T^* = \int\limits_{\mathrm{h}_f^*}^{1} W^* d\mathrm{h}_m$$

$$T^* = \int_{\mathrm{h}_f^*}^{1}\left\{\frac{3\pi}{2}\left[\frac{1}{F_0\left(h^*, l^*, \sigma^*, C\right)} - G\left[\frac{F_1\left(h^*, l^*, \sigma^*, C\right)}{\left[F_0\left(h^*, l^*, \sigma^*, C\right)\right]^3}\right]\right]\right\} d\mathrm{h}_m \tag{28}$$

3. Neural network surrogate model

In the present work, the NNSM model is employed to investigate the effects of the piezo-viscous parameter G, couple stress parameter l^*, and roughness parameter Con the squeeze film characteristics between circular plates. The neural network is well trained using the analytical solutions of pressure P^*, load-carrying capacity W^*, and response time T^*. During training, the network adjusts its weights and biases so the outputs match both the physical behavior and the provided solution data.

The developed NNSM framework consists of multiple hidden layers with nonlinear activation functions, enabling accurate approximation of highly nonlinear fluid flow behavior. The training process minimizes the mean squared error between analytical and predicted values while improving the solution's physical consistency. Performance evaluation uses regression analysis, validation performance, residual error analysis, and error histograms.

3.1. The neural network surrogate model calculations are performed through the following steps for the squeeze film lubrication

In the governing equation, the lubrication behavior is generally expressed as a nonlinear Reynolds-type differential equation involving pressure distribution P^*, the piezo-viscous parameter G, the couple stress parameter l to the *, and the roughness parameter C. The basic governing equation can be represented as $N(P^*) = 0$, where N is the nonlinear differential operator and P^* is the unknown pressure function. This equation becomes the "physics constraint" inside the NNSM. Neural Network Approximation: The neural network estimates the unknown solution as: $P_\theta^*(x)$, where x denotes input variables, θ denotes network weights and biases. The Inputs here are (G, l^*, C) and the outputs are (P^* , W^*, T^*). The neural network predicts these outputs persistently. For automatic differentiation, NNSMs use automatic differentiation to compute derivatives appearing in the governing equations. These derivatives are needed because the Reynolds equation contains differential terms. In residual calculation, the predicted pressure is substituted into the governing equation: Residual $R(r^*) = N(P_\theta^*(r^*))$. If the governing equation is perfectly satisfied, $R(r^*) = 0$. Then the NNSM minimizes this residual everywhere in the domain. The boundary conditions are also implemented $P^*(1) = 0$, at the plate edge. Boundary loss: $L_{BC} = |P_\theta^*(1) - 0|^2$. This confirms physical correctness. For data loss, the difference between analytical and NNSM predictions is $L_{data} = \frac{1}{N}\sum(y_{true} - y_{pred})^2$. This is the standard MSE loss. The total NNSM loss is the sum of the physics loss $L_{physics} = \frac{1}{N_r}\sum R(r^*)^2$, boundary loss L_{BC}, data loss L_{data}: $L_{total} = L_{\text{physics}} + L_{BC} + L_{data}$.

The network minimizes this total loss during training. During the optimization process, the optimizer iteratively updates the model's weights and biases. Common optimizers include Adam, L-BFGS, and gradient descent. The weights are updated as: $\theta_{new} = \theta_{old} - \eta\frac{\partial L}{\partial \theta}$ where η is the learning rate.

After getting the pressure prediction $W^* = \int_0^1 2r^*P^*dr^*$, the NNSM-predicted pressure is numerically integrated to compute load and calculate load-carrying capacity. Response time is obtained from squeeze film relations using predicted pressure/load values.

The obtained root mean square error (RMSE) and coefficient of determination (R^2) values indicate that the developed NNSM predicts the squeeze film characteristics with extremely high precision and excellent agreement with the analytical solutions. The RMSE measures the average deviation between the analytical results and the NNSM predictions. Smaller RMSE values indicate better predictive capability of the neural network model. In the present study, the RMSE values for pressure, load-carrying capacity, and response time are extremely small, namely pressure RMSE = 0.0286513525, load RMSE = 0.0450488624, time RMSE = 0.0000197129. These extremely low error values confirm that the NNSM model accurately captures the nonlinear behavior of the lubrication system. In particular, the extremely small RMSE obtained for the response time demonstrates the strong capability of the model in predicting transient squeeze film characteristics with negligible deviation from the analytical solution.

The R^2 evaluates how well the predicted outputs fit the analytical data. An R^2 value closer to 1 indicates better correlation between the predicted and actual values. The obtained values are pressure $R^2 = 0.9999965579$, load $R^2 = 0.9999983940$, and time $R^2 = 0.9999975229$. These values are remarkably close to unity, indicating almost perfect agreement between the analytical answers and NNSM predictions. This confirms that the trained NNSM model learned the underlying physical behavior governed by the lubrication equations and accurately reproduced the pressure distribution, load-carrying capacity, and response-time characteristics.

4. Results and discussion

Based on the stochastic theory of Christensen[15] and Barus,[1] one can evaluate the medium's permeability for couple-stress fluids by applying the approximation proposed by Morgan and Cameron. By examining two different roughness patterns, the study assesses how surface roughness influences the lubrication performance of couple-stress fluids between circular plates. The squeeze-film features are examined using several nondimensional factors, including the couple-stress factor l^*, load-bearing capacity W^*, pressure P^*, squeeze-film time T^*, and radial coordinate r^*. These parameters depend on the slip velocity parameter (σ), pressure-sensitive viscosity (G), and roughness parameter (C). In the following discussion, we investigate the squeeze-film properties of rough circular plates.

The current study aligns with earlier work by Lin *et al.*[12] when slip velocity and roughness are absent. Nevertheless, when viscosity values of 0, 0.02, 0.04, and 0.06 were taken into account along with a slip velocity value of 0.2 and a roughness parameter of 0.3, the appropriate load values were 3.167, 3.19351, 3.22001, and 3.24652 (radial values), also 3.50198, 3.53297, 3.56396, and 3.59495 (azimuthal values), respectively. These findings suggest that viscosity increases the load. Likewise, with identical slip velocity and viscosity, the squeeze times were 17.2623, 19.9646, 22.667, and 25.3693 (radial values) and 90.2525, 107.631, 125.009, and 142.387 (azimuthal values), suggesting that squeeze time also increases. In addition, for a slip velocity of 0.4 and the same roughness parameter of 0.3, **Table 1** shows that both squeeze time and load capacity increased steadily with radial and azimuthal roughness. Minor fluctuations were also noted, suggesting that couple-stress fluids are superior lubricants.

4.1. Pressure distribution

Figure 2 illustrates how the radial coordinate r^* affected the dimensionless pressure P^* for distinct values of l^*. The radial and azimuthal roughness configurations corresponded for both rough surfaces, and increasing azimuthal roughness resulted in significantly higher pressures, especially at larger correlation lengths. At $l^* = 0.6$, the pressure peaked above 250 near the center ($r^* = 0$), then gradually decreased toward the outer radius. **Figure 3** displays the radial axis r^* and the dimensionless pressure variation with different values of pressure-dependent viscosity G. It was noted that in both the radial and azimuthal cases, the pressure increased noticeably for varying values of G. **Figure 4** displays the radial axis r^* and the variation of dimensionless pressure for various values of roughness parameter C. For both rough surfaces, it was found that the radial and azimuthal roughness configurations coincide at $C = 0.0$. Furthermore, as C increases, the dimensionless pressure decreased in radial roughness but increased in azimuthal roughness. **Figure 5** displays the radial axis r^* and the variation of dimensionless pressure for various values of slip velocity σ. It was noted that the pressure decreased substantially for different values of slip velocity (σ) in both radial and azimuthal cases.

Physically, couple stress and pressure-dependent viscosity improve the lubricant's ability to generate pressure by increasing its internal resistance to deformation and flow, while azimuthal roughness and longer correlation lengths further obstruct radial flow and reinforce this pressure buildup. Conversely, radial roughness, higher roughness magnitude in the radial configuration, and slip velocity all facilitate easier fluid escape and reduce flow resistance. Consequently, pressure generation is reduced.

4.2. Load-carrying capacity

Figure 6 illustrates how nondimensional load W^* varied with the nondimensional film thickness h_m^* for various l^* values. In radial roughness, couple stress increased; the load decreased sharply with increasing film thickness. In azimuthal roughness, the load-carrying capacity was much higher, exceeding 350, while radial roughness remained much lower. In **Figure 7**, for various values of pressure-dependent viscosity G for both roughness patterns, the load increased noticeably. **Figure 8** shows the relationship between W^* and h_m^* for various C values. The load-carrying capacity improved with azimuthal roughness while decreasing with radial roughness as the roughness parameter increased. Additionally, **Figure 9** shows how nondimensional W^* varied with nondimensional h_m^* for different slip velocity (σ) values for both roughness cases. In radial roughness, the load-carrying capacity decreased as slip velocity increased, and in azimuthal roughness, the load-carrying capacity decreased. It was demonstrated that for circular plates, an increase in slip velocity resulted in an improvement in the average load-carrying capacity as compared to a smooth plate scenario. Physically, wider film thickness, radial roughness, and slip velocity facilitate and lessen fluid escape, while couple stress, pressure-dependent viscosity, and azimuthal roughness improve flow resistance and increase load capacity (aided by longer correlation lengths and greater roughness). On average, rough surfaces still perform better than smooth ones.

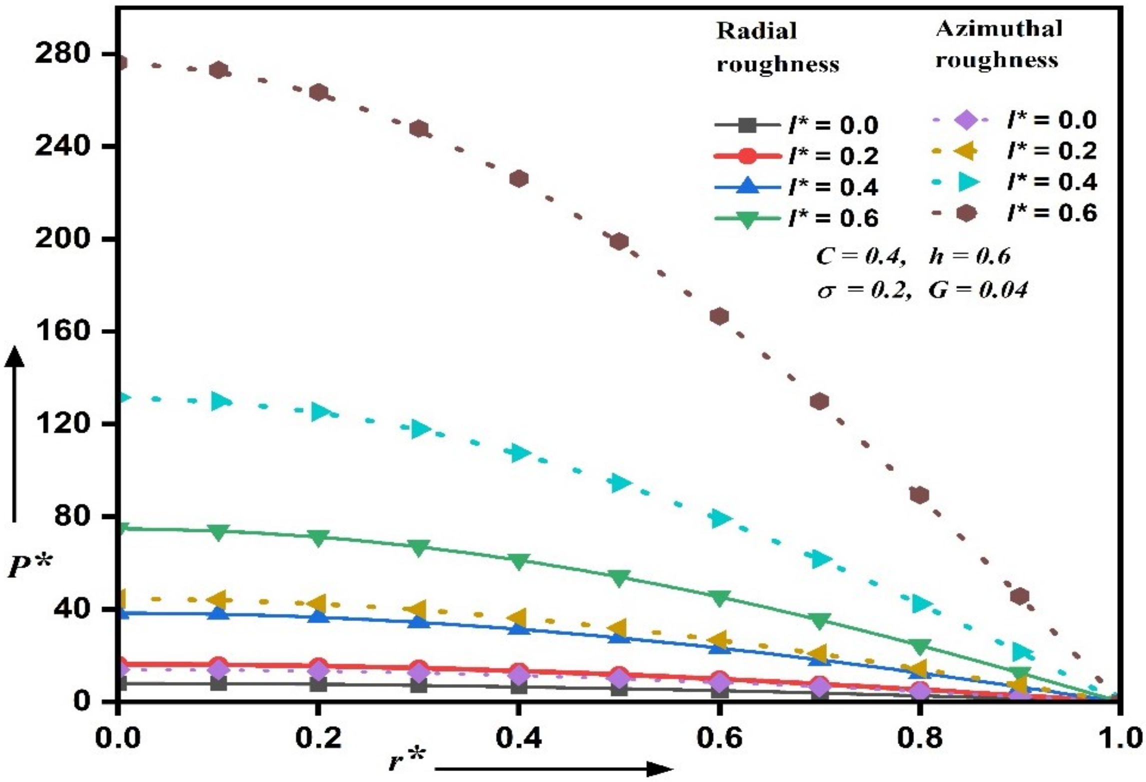

Figure 2. Graphical analysis of P^*versus r^* for a range of l^*values

4.3. Squeezing film time

The nondimensional response time for the squeeze film T^*, with nondimensional film thickness h_f^* is shown in **Figure 10** for several l^* values. For radial and azimuthal roughness, the squeeze-film time increased as the couple-stress parameter increased. At $l^* = 0$, both roughnesses coincided. Also, the nondimensional response of the squeeze-film time T^* with nondimensional film thickness h_f^* is shown in **Figure 11** for a few G values. The squeeze-film duration increased with slip velocity for both radial and azimuthal roughness. **Figure 12** shows the nondimensional response squeeze-film time T^* with nondimensional film thickness h_f^* for various C values. In radial roughness, the roughness parameter increased. The squeeze-film time decreased, and in azimuthal roughness, it increased. The relationship between dimensionless squeeze-film time T^* and nondimensional film thickness h_f^* is shown in **Figure 13** for several slip-velocity values in both roughness cases. In radial roughness, slip velocity increased and squeeze-film time decreased; in azimuthal roughness, squeeze-film time also decreased. Physically, couple stress, pressure-dependent viscosity, and azimuthal roughness enhance the lubricant's resistance to deformation and outflow, thereby prolonging squeeze-film response time and improving film stability. On the other hand, slip velocity reduces boundary drag, allowing outflow, and radial roughness speeds drainage through simpler flow channels, both of which reduce squeeze-film time in any configuration.

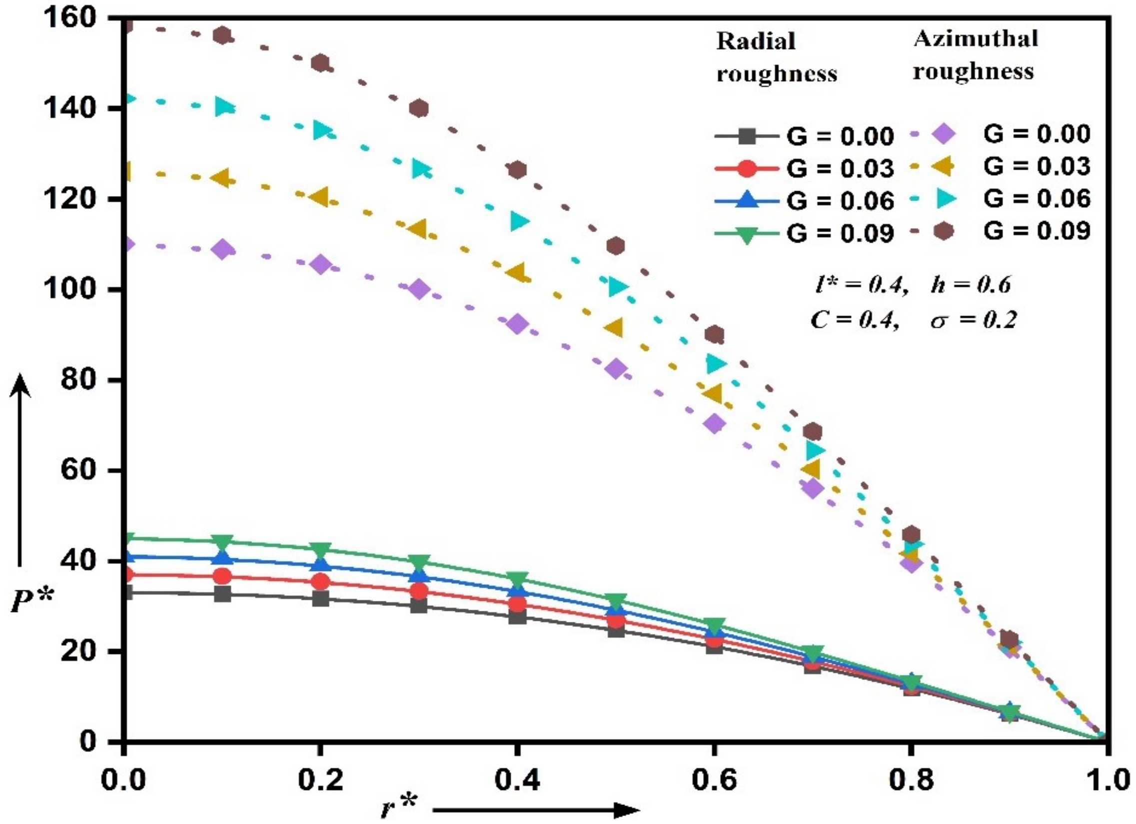

Figure 3. Graphical analysis of $P^{*}versus\ r^{*}$ for a range of G values

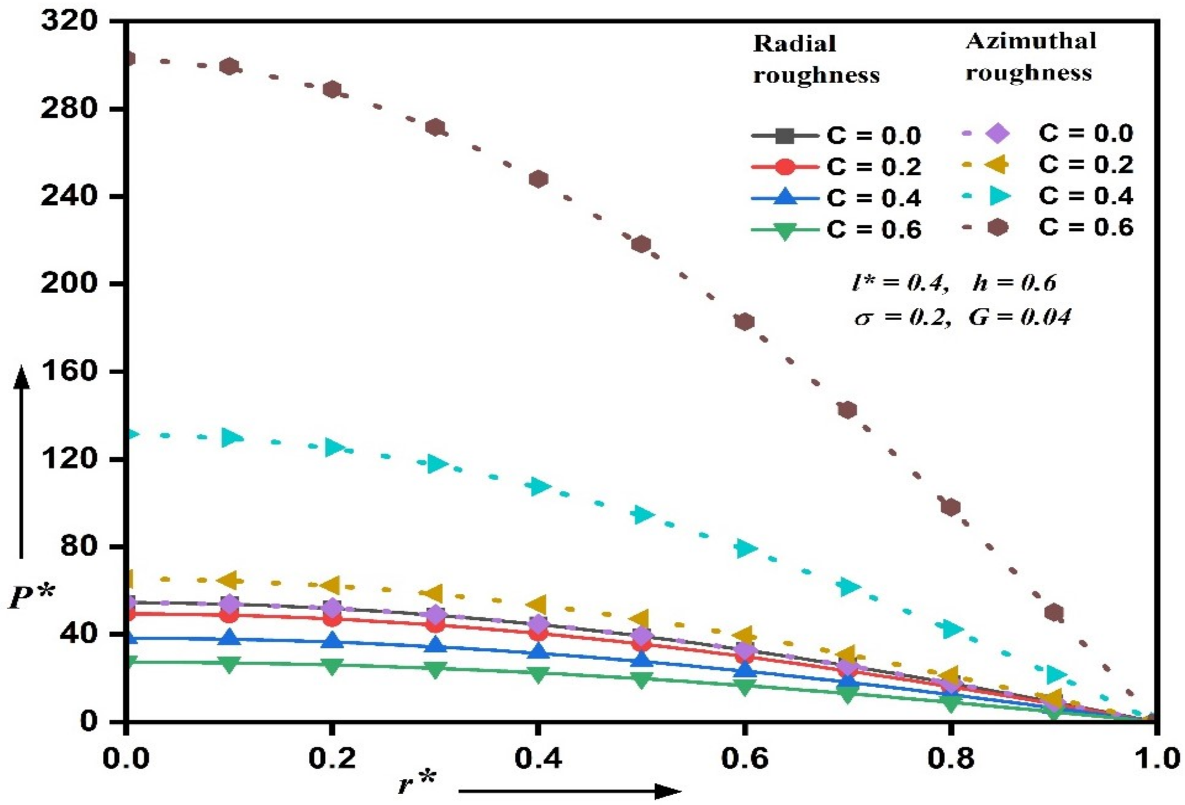

Figure 4. Graphical analysis of P^{*}versus r^{*} for a range of C values

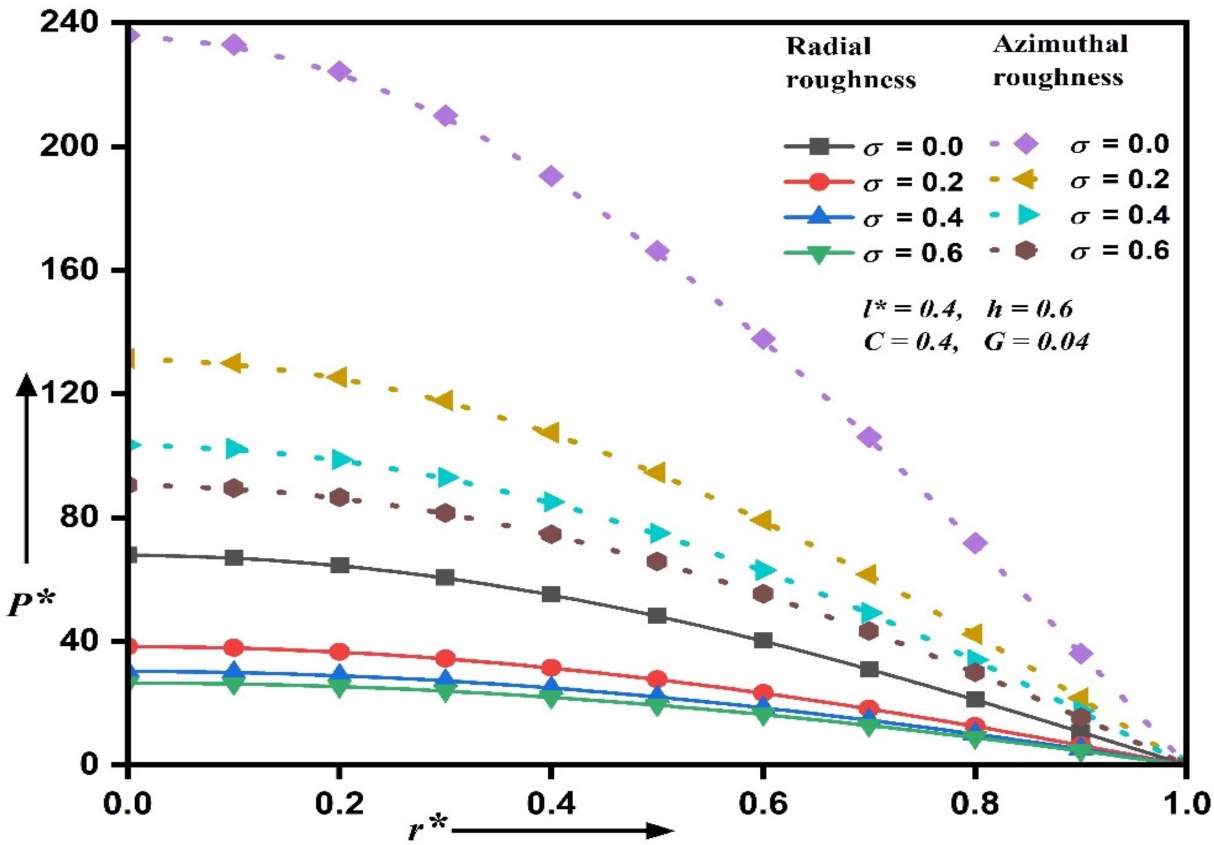

Figure 5. Graphical analysis of P^*versus r^* for a range of σ values

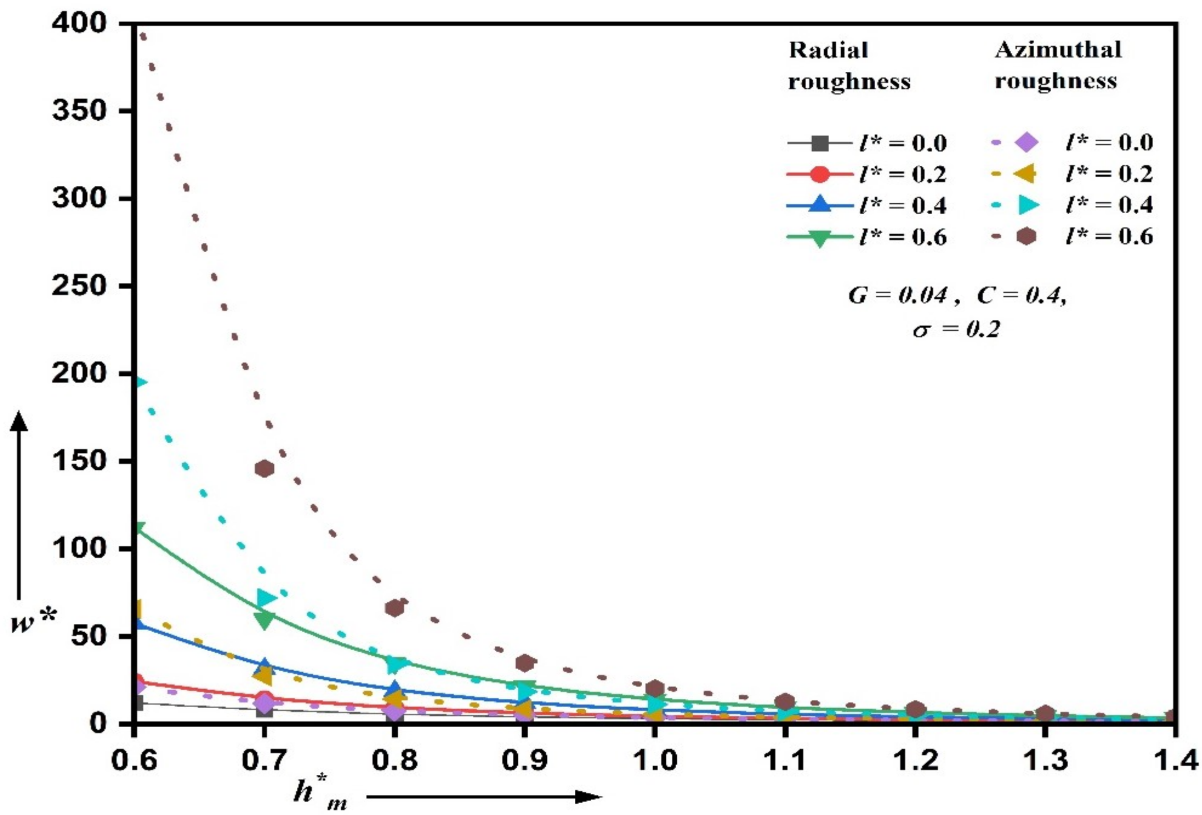

Figure 6. Graphical analysis of w^*versus h_m^* for a range of l^* values

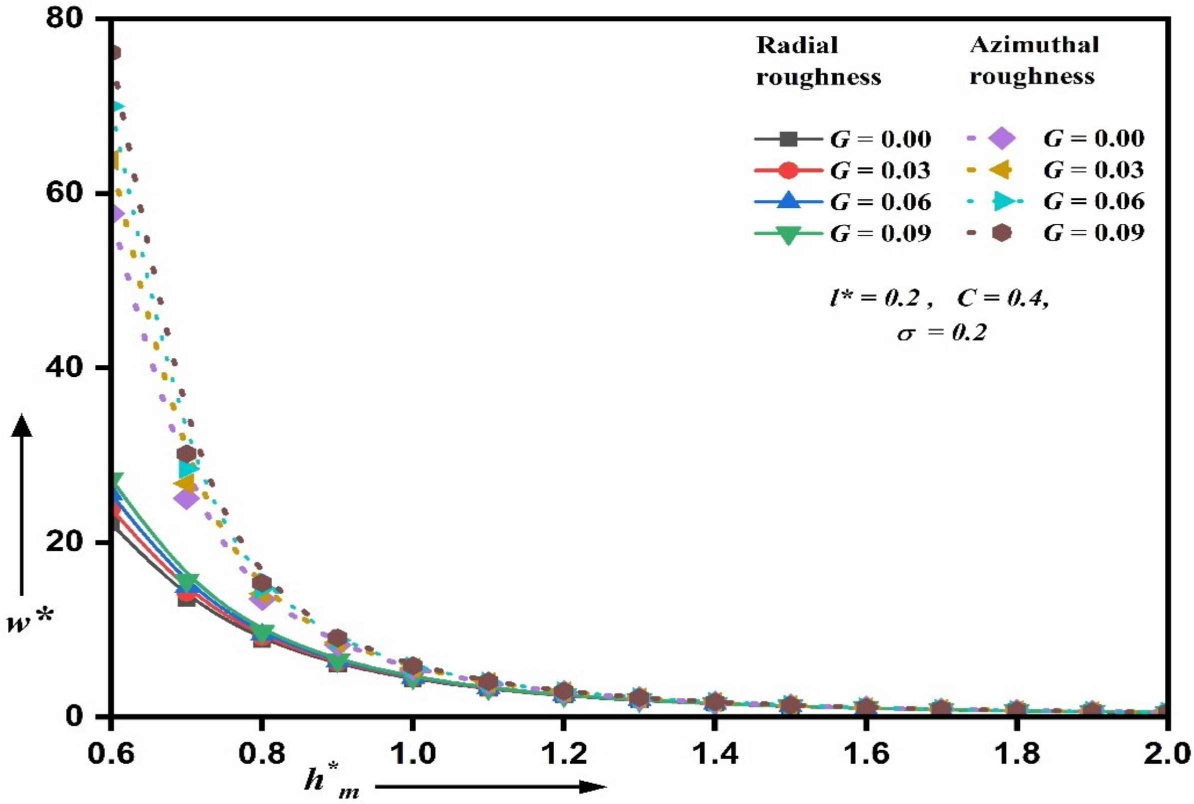

Figure 7. Graphical analysis of w^*versus h_m^* for a range of G values

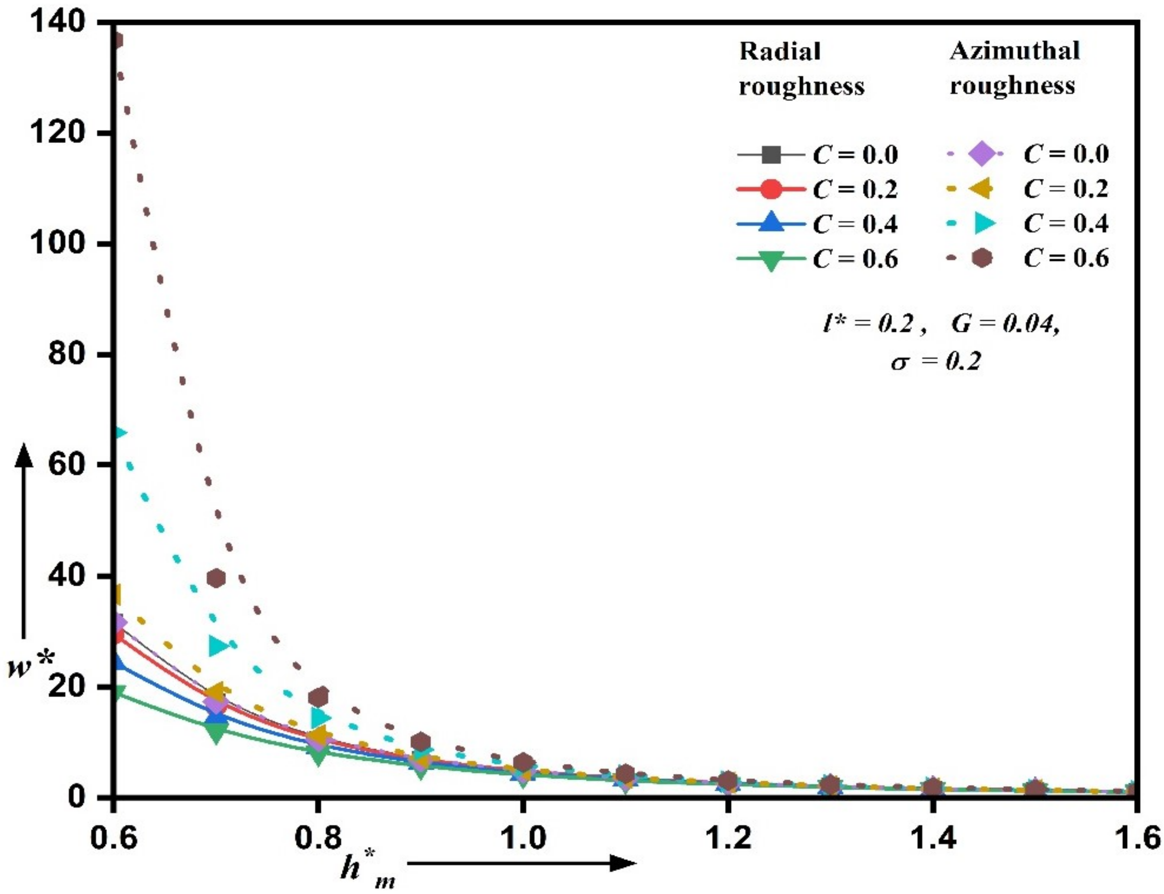

Figure 8. Graphical analysis of w^*versus h_m^* for a range of C values

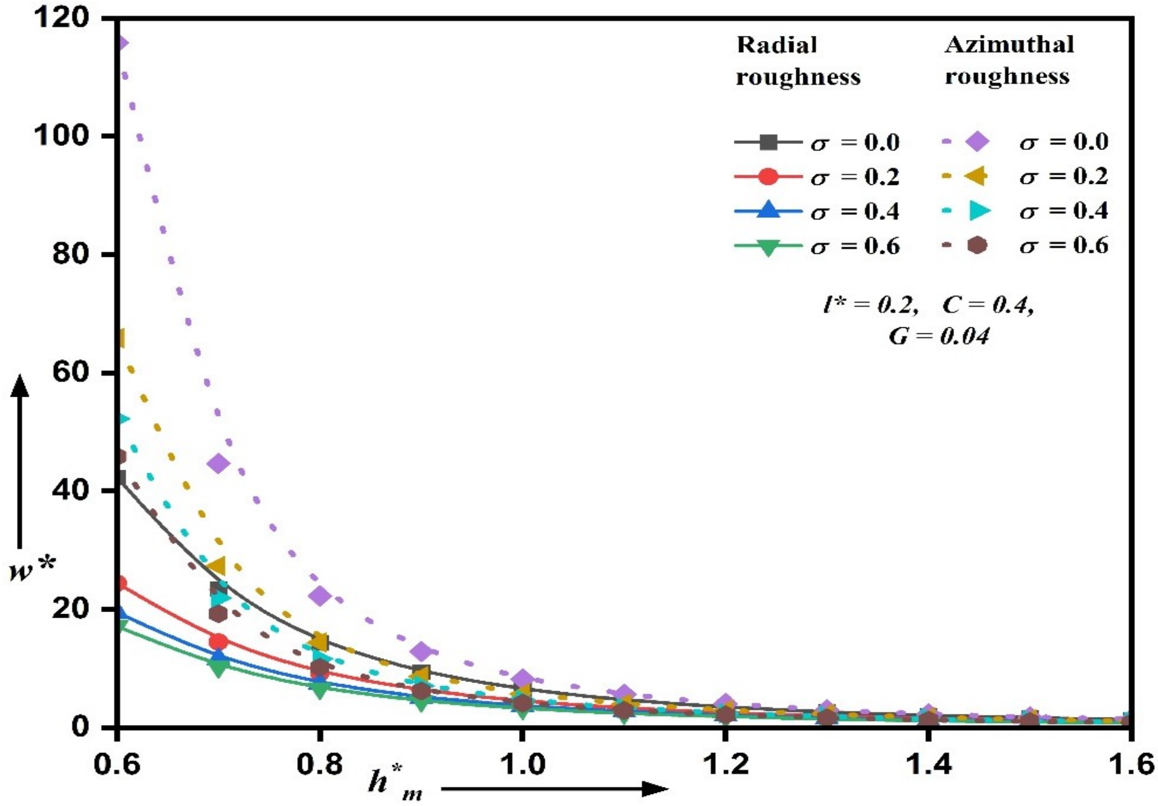

Figure 9. Graphical analysis of w^*versus h_m^* for a range of σ values

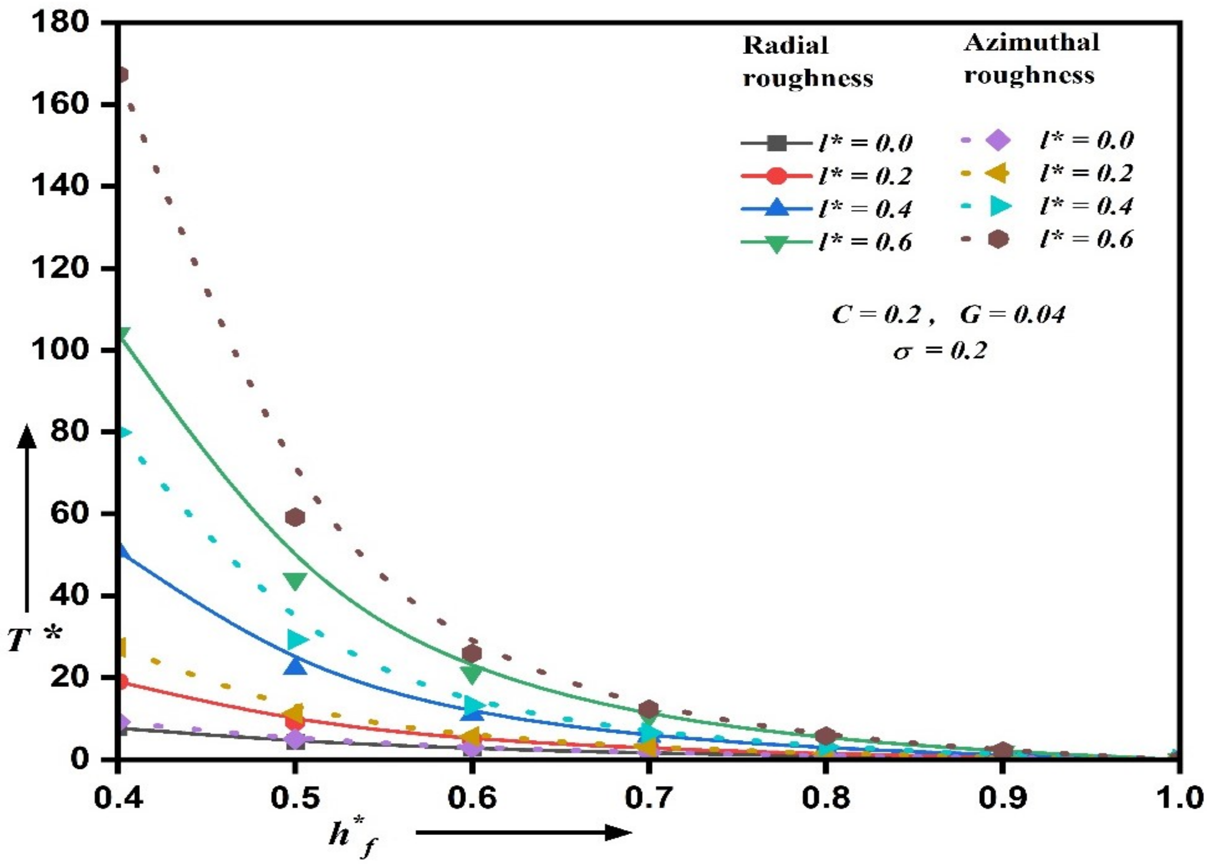

Figure 10. Graphical analysis of T^*versus h_f^* for a range of l^* values

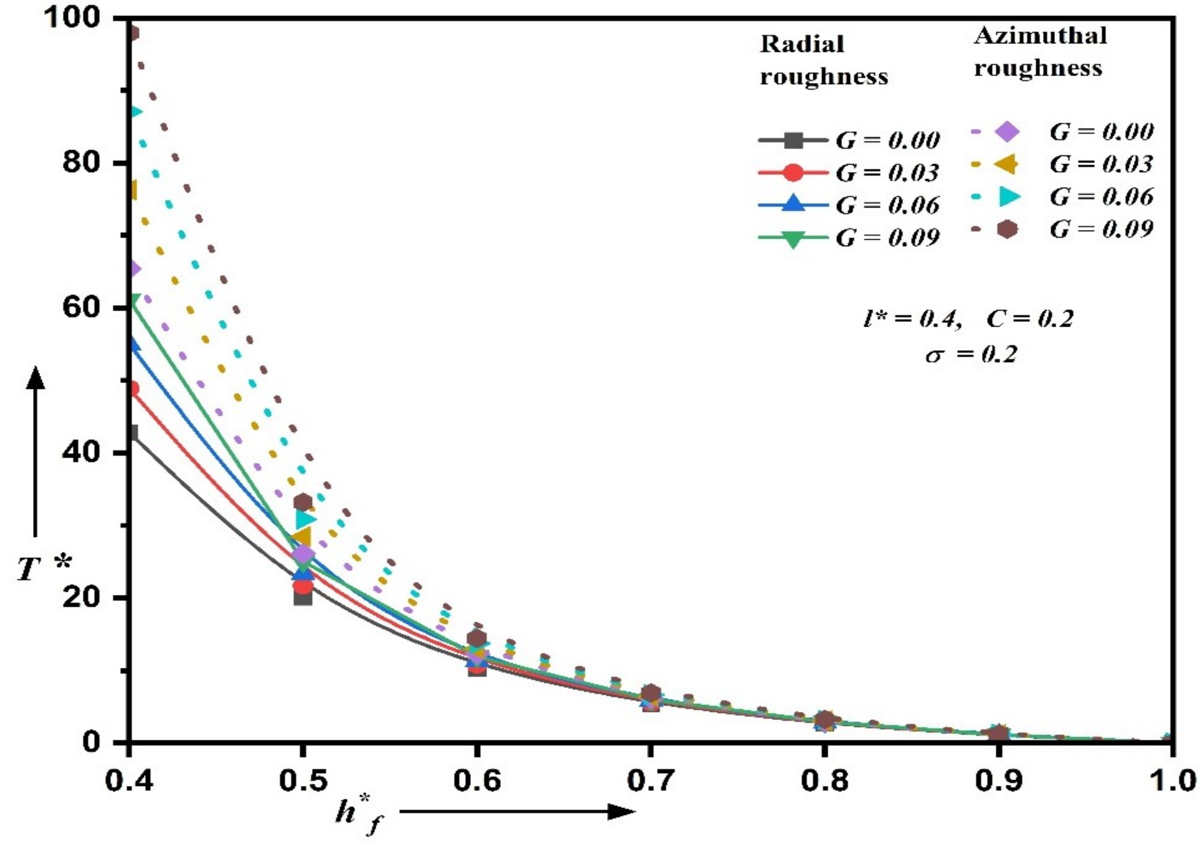

Figure 11. Graphical analysis of T^*versus h_f^* for a range of G values

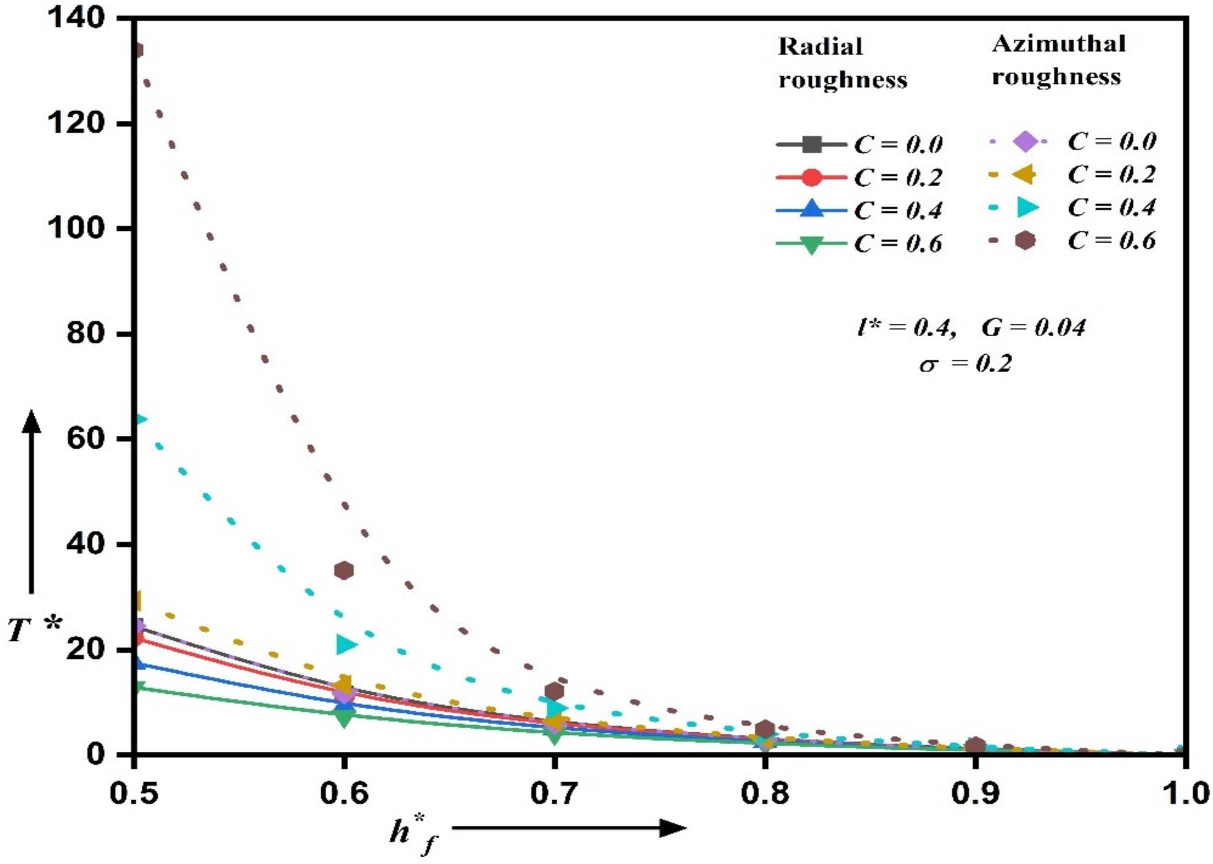

Figure 12. Graphical analysis of T^*versus h_f^* for a range of C values

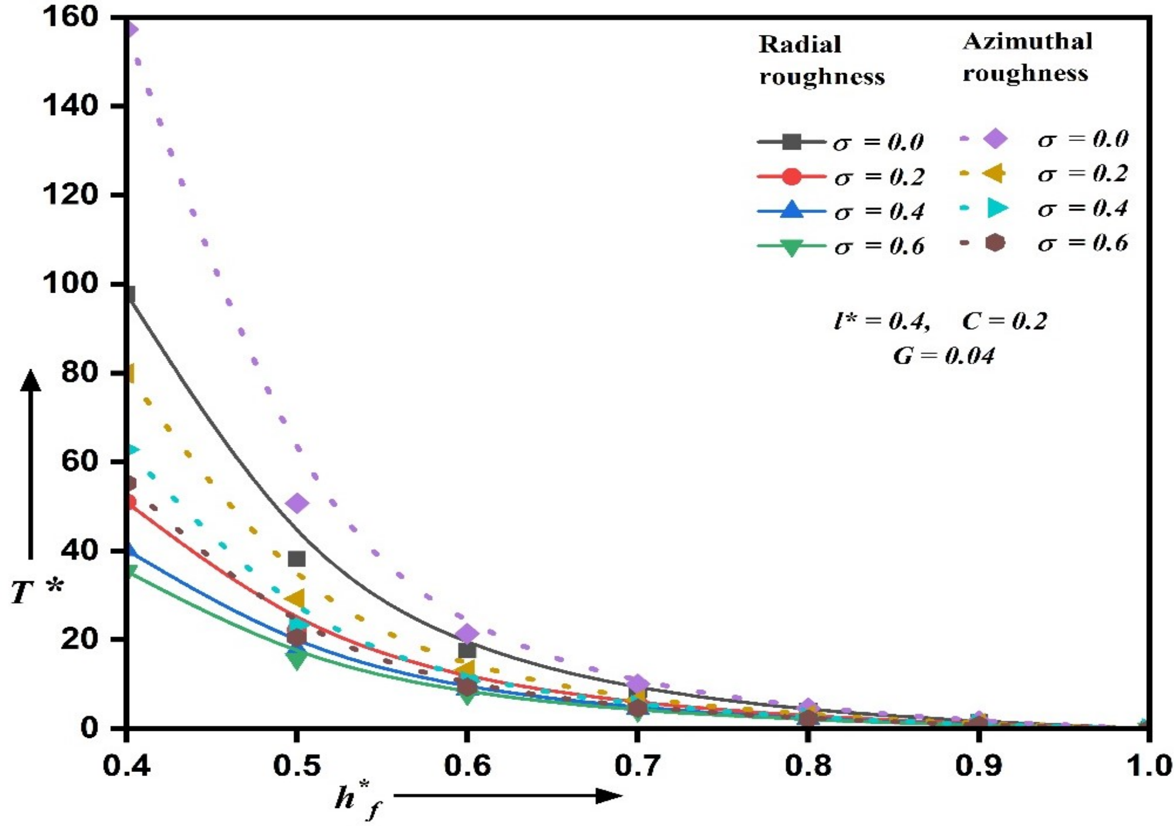

Figure 13. Graphical analysis of T^*versus h_f^* for a range of σ values

4.4. Enhanced neural network surrogate model error histogram

Figure 14 illustrates the distribution of prediction errors between the analytical and NNSM solutions. Most errors were close to zero, indicating that most predictions deviate only slightly from the exact analytical values. The histogram's narrow spread shows that the trained NNSM model was numerically stable and consistent across the dataset. The absence of large error tails further illustrates that the model did not suffer from significant overfitting or unstable predictions. Therefore, the histogram validates the excellent generalization capability of the proposed NNSM approach.

4.5. Best validation performance

Figure 15 shows the variation of validation loss with training epochs. Initially, the validation error decreased rapidly, showing that the network effectively learned the nonlinear relationship between the governing parameters and the physical outputs. As training progressed, the validation loss converged toward a small value near zero, indicating successful optimization of the network weights. The minimum validation loss corresponded to the optimal network state, maximizing prediction accuracy without overtraining. The smooth convergence behavior demonstrates the stability of the training process and indicates that the selected network architecture and training parameters are appropriate for the present lubrication problem.

4.6. Three-dimensional error surface

The three-dimensional error surface plot (**Figure 16**) shows how prediction errors varied between the analytical and NNSM solutions for different parameters, such as pressure and load-carrying capacity, under various operating conditions. The x-axis represents the data samples corresponding to various combinations of the piezo-viscous parameter G, couple stress parameter l^* and roughness parameter C. The y-axis denotes the absolute pressure error, while the z-axis represents the absolute load error. The surface remained near the zero-error plane throughout the computational domain, indicating excellent agreement between the analytical and NNSM solutions. The maximum observed errors are extremely small, confirming the robustness, stability, and high predictive capability of the proposed NNSM framework prepared for modeling squeeze film lubrication characteristics. The plotted quantities are: $P_{Error} = |P_{Analytical} - P_{NNSM}|$ and $W_{Error} = |W_{Analytical} - W_{NNSM}|$ The nearer the values are to zero, the better the NNSM model performance.

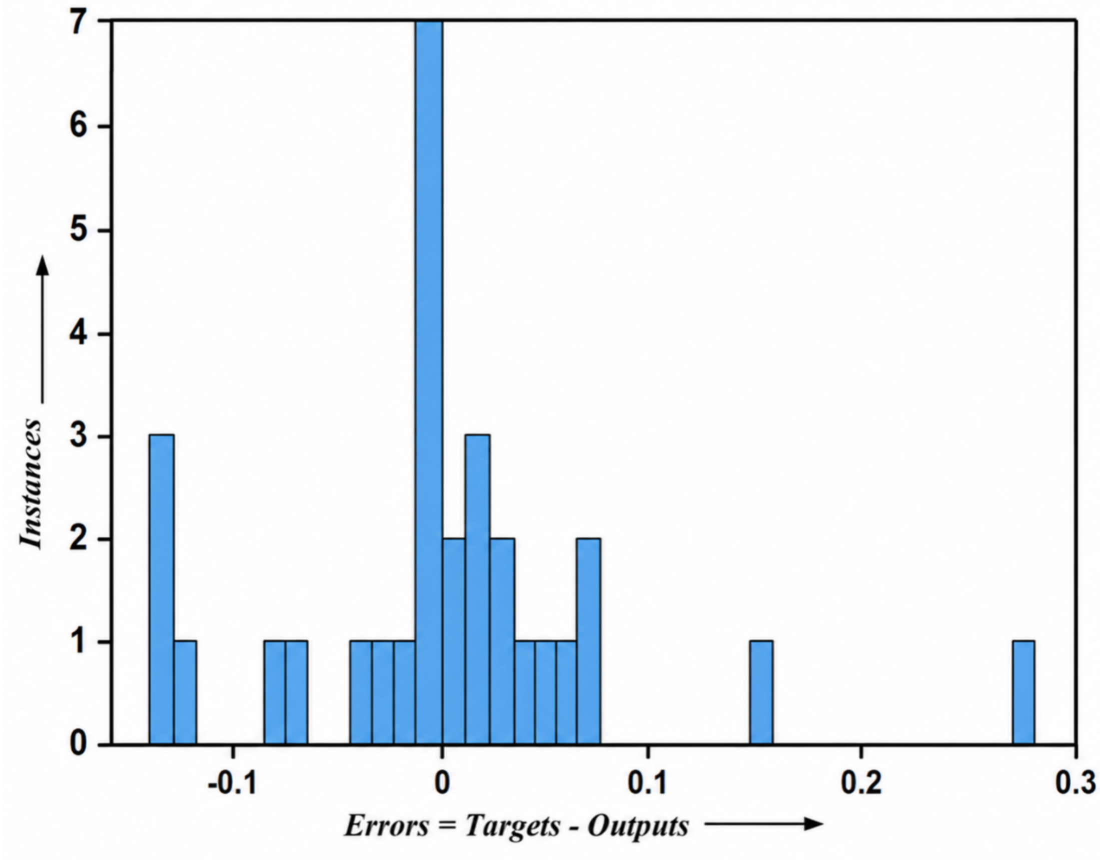

Figure 14. Enhanced neural network surrogate model error histogram

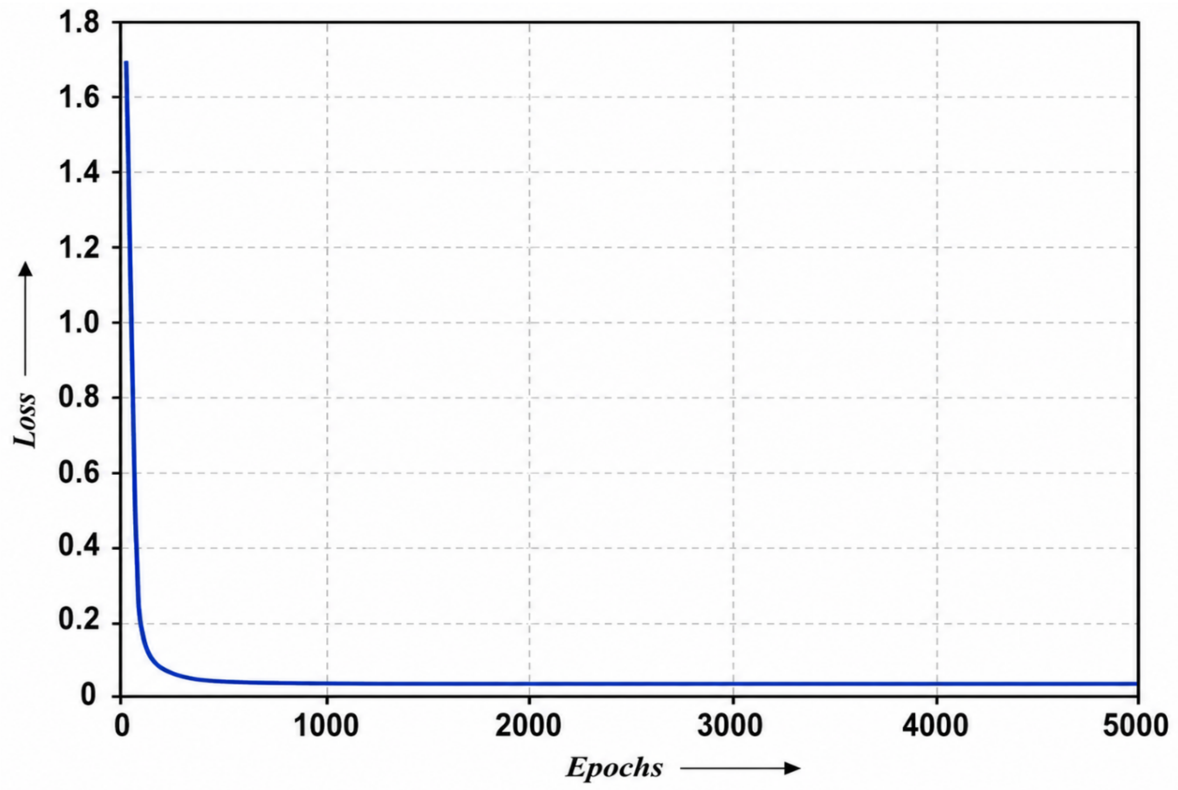

Figure 15. Best validation performance

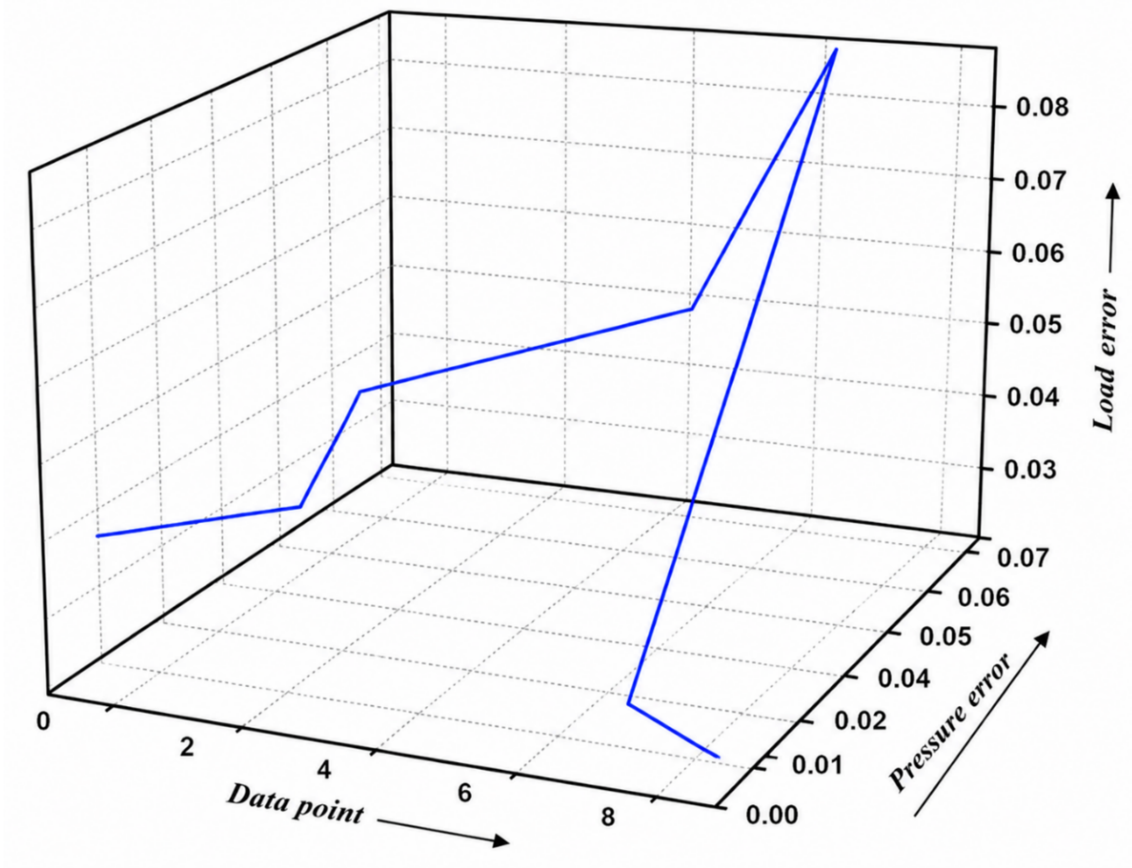

Figure 16. Three-dimensional error surface

4.7. Residual error plot

The residual error plot (**Figure 17**) shows the deviation between the analytical solutions and the predicted values obtained from the NNSM model for pressure P^*, load-carrying capacity W^*, and response time T^*. The residual error was calculated as Residual Error = |Analytical Solution − NNSM Prediction|. The plot demonstrates that the residual errors were extremely small throughout all computational points, confirming the valuable predictive capability of the NNSM framework for the pressure distribution P^*. The residual error was close to zero for most data points, with near-exact agreement between the analytical and NNSM solutions. The maximum pressure error was approximately 0.072, which is negligible compared to the magnitude of the pressure values. Similarly, the load-carrying capacity showed low deviations, with errors remaining below 0.1. The errors do not oscillate and are uniformly distributed, indicating stable convergence of the NNSM model. For the response time T^*, the residual errors were of the order 10^{-5}. It validates the network's high degree of numerical precision. Overall, the residual error figure confirms that the analytical solutions and NNSM predictions coincide well, confirming the correctness, stability, and resilience of the suggested computational model for squeeze film lubrication investigation.

4.8. Regression analysis error plot

Figure 18 compares the analytical outputs with the NNSM predicted outputs. The data points exhibited an outstanding correlation between the exact and predicted values, since they lie nearly exactly along the 45° reference line. The regression coefficient R was close to unity, confirming that the developed NNSM model has almost exact predictive performance. This demonstrates that the network successfully recalculated the analytical characteristics of pressure, load-carrying capacity, and response time with high precision.

Table 1 compares the current analysis with the earlier analysis by Lin *et al.*[12] The table shows that the load for both roughness patterns has significantly increased. An increase of 3.20%/3.39% in the radial/azimuthal pattern of roughness was observed for $G = 0.06$, $h = 1.2$, $\sigma = 0.2$, $C = 0.3$. Additionally, the squeeze film time increased considerably for both roughness types, as shown in **Table 1**. An increase of 25.36%/142.38% was observed for a pattern of radial and azimuthal roughness for $G = 0.06$, $h = 0.8$, $\sigma = 0.2$, $C = 0.3$.

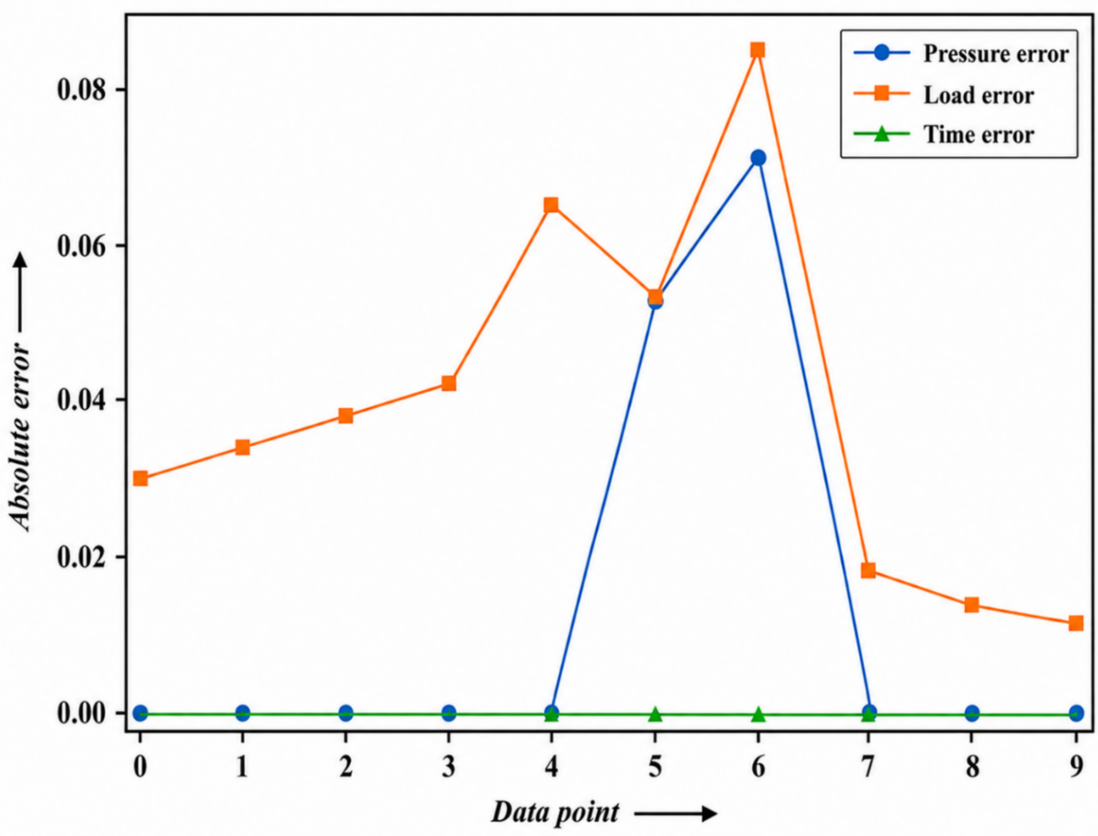

Figure 17. Residual error plot

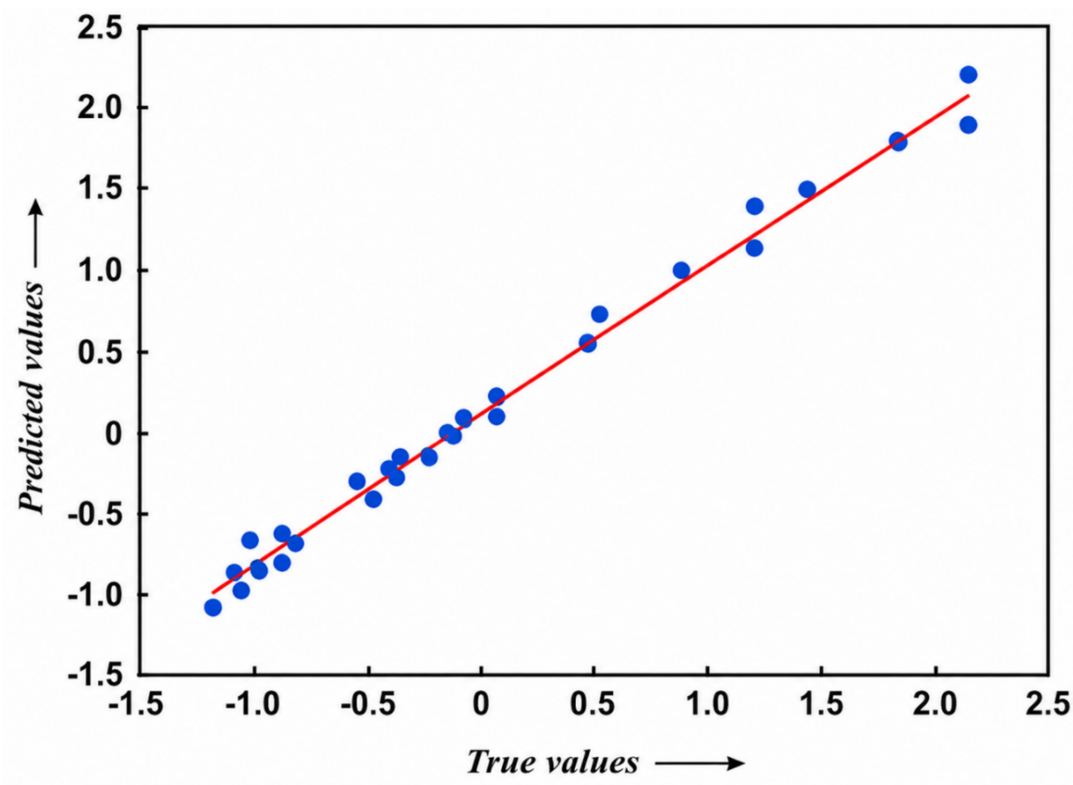

Figure 18. Regression analysis error plot

Table 1. Load-carrying capacity W^* as well as squeeze film time T^* compared between Lin *et al.*[12] and the current analysis using fixed $l^* = 0.3$

Lin *et al.*[12] analysis				Present analysis			
				Radial	**Azimuthal**	**Radial**	**Azimuthal**
$C = 0$				$C = 0.3$	$C = 0.3$	$C = 0.3$	$C = 0.3$
$\sigma = 0$				$\sigma = 0.2$	$\sigma = 0.2$	$\sigma = 0.4$	$\sigma = 0.4$
	G	$h = 1.2$	$h = 1.2$	$h = 1.2$	$h = 1.2$	$h = 1.2$	$h = 1.2$
	0.00	4.45958	4.45958	3.16700	3.50198	2.63946	2.91917
	0.02	4.51165	4.51165	3.19351	3.53297	2.65782	2.94064
	0.04	4.56373	4.56373	3.22001	3.56396	2.67618	2.96211
	0.06	4.6158	4.6158	3.24652	3.59495	2.69454	2.98359
w^*	G	$h = 1.5$	$h = 1.5$	$h = 1.5$	$h = 1.5$	$h = 1.5$	$h = 1.5$
	0.00	1.96815	1.96815	1.48479	1.57272	1.2553	1.32983
	0.02	1.9799	1.9799	1.49148	1.58008	1.26007	1.33507
	0.04	1.99166	1.99166	1.49817	1.58744	1.26483	1.34032
	0.06	2.00341	2.00341	1.50486	1.5948	1.2696	1.34557
	G	$h = 0.4$	$h = 0.4$	$h = 0.4$	$h = 0.4$	$h = 0.4$	$h = 0.4$
	0.00	48.8667	48.8667	17.2623	90.2525	14.8611	73.532
	0.02	64.3131	64.3131	19.9646	107.631	15.8514	85.0528
	0.04	79.7596	79.7596	22.667	125.009	17.6418	96.5735
	0.06	95.206	95.206	25.3693	142.387	19.4322	108.094
T^*	G	$h = 0.8$	$h = 0.8$	$h = 0.8$	$h = 0.8$	$h = 0.8$	$h = 0.8$
	0.00	2.22492	2.22492	1.35029	1.78888	1.10359	1.46239
	0.02	2.31274	2.31274	1.38449	1.83906	1.12639	1.49586
	0.04	2.40055	2.40055	1.41869	1.88924	1.14918	1.52932
	0.06	2.48837	2.48837	1.45289	1.93942	1.17198	1.56278

Table 2 compares the analytical solutions and NNSM predictions for the nondimensional parameters: pressure P^*, load-carrying capacity W^* and time T^*under the influence of different parameters G, l^* and$C$. The results show excellent agreement between the analytical and NNSM solutions across all parameter variations, confirming the accuracy and reliability of the proposed NNSM framework. For increasing values of the piezo-viscous parameter G, the dimensionless pressure P^* and load-carrying capacity W^* increased significantly, whereas the squeeze time T^* decreased slightly. This behavior shows that a stronger pressure-dependent viscosity reduces the lubricant film stiffness and improves the load-supporting capability of the squeeze film. The influence of the couple stress parameter l^* shows that a higher value of l^* considerably increased both P^* and W^*, while decreased T^*. This enhancement occurred because the couple-stress effects increased the effective resistance to flow, strengthening the lubricant film and improving bearing performance. In contrast, increasing the roughness parameter C decreased the pressure distribution and load-carrying capacity, as the squeeze film time increased. The reduction in P^* and W^* was linked to disturbances in fluid motion caused by surface roughness, which weakens the squeeze-film action. Improved frictional and dissipative effects within the lubricant layer cause the corresponding rise in time. Overall, **Table 2** shows that the NNSM predictions closely follow the analytical solutions with negligible deviation, validating the effectiveness of the NNSM approach for analyzing squeeze-film lubrication problems involving piezo-viscous and couple-stress fluid effects.

Table 3 presents the analytical and NNSM-predicted values of dimensionless pressure (P^*), load-carrying capacity (W^*) and response time (T^*), along with their corresponding absolute and percentage errors. From **Table 3**, the NNSM predictions agree well with the analytical solutions for all cases considered. The analytical results and the pressure levels predicted by the NNSM nearly exactly match, with only marginal inaccuracy. The maximum pressure percentage error was approximately 0.13%, validating the strong predictive capability of the developed NNSM model. Similarly, the load-carrying capacity obtained through the NNSM closely matched the analytical values. For most data points, the percentage error in load remained below 0.1%, suggesting that the neural network effectively represents the lubrication system's nonlinear behavior. Even at larger load magnitudes, the discrepancy between analytical and NNSM solutions remained negligible. For the response time parameter, the NNSM predictions also demonstrated remarkable accuracy. The absolute errors were on the order of 10^{-5}, while the percentage errors remained below approximately 0.32%. These small variations indicate that the trained network has captured the fundamental physical properties governing the squeeze film lubrication problem. Overall, the low error magnitudes and close agreement between analytical and NNSM results validate the robustness, reliability, and computational efficiency of the proposed NNSM framework. The findings verify that the NNSM model can accurately estimate the governing lubrication equations with great numerical precision.

Table 2. The analytical and neural network surrogate model (NNSM) comparison of pressure, load, and time values for different G, l^*, and C values

Variables		P^*_analytical	P^*_NNSM	W^*_analytical	W^*_NNSM	T^*_analytical	T^*_NNSM
G	0.00	13.889	13.889	33.51	33.48	0.017386	0.017401
	0.03	16.782	16.782	37.978	37.944	0.015393	0.015407
	0.06	19.676	19.676	42.446	42.408	0.01381	0.013822
	0.09	22.569	22.569	46.914	46.872	0.012522	0.012533
l^*	0.0	13.889	13.889	33.51	33.48	0.017386	0.017401
	0.2	29.473	29.473	71.111	71.046	0.008321	0.008328
	0.4	41.256	41.201	95.334	95.28	0.005214	0.005228
	0.6	55.842	55.77	128.445	128.36	0.003812	0.003824
C	0.0	13.889	13.889	33.51	33.48	0.017386	0.017401
	0.2	7.9365	7.9365	19.149	19.131	0.029779	0.029804
	0.4	6.3131	6.3131	15.232	15.218	0.036964	0.036995
	0.6	5.5556	5.5556	13.404	13.392	0.041655	0.04169

Table 3. Comparison of analytical and neural network surrogate model (NNSM) predicted values

P^*_analytical	P^*_NNSM	W^*_analytical	W^*_NNSM	T^*_analytical	T^*_NNSM
13.889	13.889	33.51	33.48	0.017386	0.017401
16.782	16.782	37.978	37.944	0.015393	0.015407
19.676	19.676	42.446	42.408	0.013810	0.013822
22.569	22.569	46.914	46.872	0.012522	0.012533
29.473	29.473	71.111	71.046	0.008321	0.008328
41.256	41.201	95.334	95.280	0.005214	0.005228
55.842	55.770	128.445	128.36	0.003812	0.003824
7.9365	7.9365	19.149	19.131	0.029779	0.029804
6.3131	6.3131	15.232	15.218	0.036964	0.036995
5.5556	5.5556	13.404	13.392	0.041655	0.041690
P^*_error	W^*_error	T^*_error	P^*_%error	W^*_%error	T^*_%error
0.000	0.030	1.5×10^{-05}	0.000000	0.089526	0.086276
0.000	0.034	1.4×10^{-05}	0.000000	0.089526	0.090950
0.000	0.038	1.2×10^{-05}	0.000000	0.089526	0.086894
0.000	0.042	1.1×10^{-05}	0.000000	0.089526	0.087845
0.000	0.065	7.0×10^{-06}	0.000000	0.091406	0.084125
0.055	0.054	1.4×10^{-05}	0.133314	0.056643	0.268508
0.072	0.085	1.2×10^{-05}	0.128935	0.066176	0.314795
0.000	0.018	2.5×10^{-05}	0.000000	0.094000	0.083952
0.000	0.014	3.1×10^{-05}	0.000000	0.091912	0.083865
0.000	0.012	3.5×10^{-05}	0.000000	0.089526	0.084024

5. Conclusion

This study presents the interaction of slip velocity and piezo-viscous effects in couple-stress fluid flow over Rough circular plates, based on the rough-surface Christensen Stochastic theory.[15] The following conclusions were drawn from the theoretical and numerical results.

- A comprehensive squeeze film lubrication model was developed by simultaneously incorporating slip velocity, pressure-dependent viscosity, couple-stress fluid behavior, and Christensen's stochastic surface roughness model for rough circular plates.
- Unlike previous studies, the present work integrates all these physical effects within a single analytical framework and employs an NNSM-based surrogate model for efficient prediction of lubrication characteristics.
- The dimensionless pressure, load-carrying capacity, and squeeze film response time increase with increasing couple stress parameter and pressure-dependent viscosity parameter for both radial and azimuthal roughness patterns.
- Increasing the slip velocity parameter reduces the pressure distribution, load-carrying capacity, and squeeze film response time due to reduced fluid resistance at the solid boundaries.
- Azimuthal roughness improves lubrication performance, whereas radial roughness decreases pressure generation, load support, and squeeze film response time compared with the smooth surface case.
- The developed analytical results show excellent agreement with the published results of Lin et al., confirming the validity and accuracy of the proposed mathematical model.
- The minimal errors exhibit the ability of NNSMs to solve intricate systems of ordinary differential equations accurately.
- The proposed NNSM surrogate model accurately predicts pressure distribution, load-carrying capacity, and squeeze film response time with absolute errors of the order of 10^{-5}, percentage errors below approximately 0.32%, low RMSE, high R^2 values and rapid convergence.
- The obtained RMSE and R^2 values demonstrate the robustness, reliability, and predictive efficiency of the proposed NNSM framework for analyzing squeeze film lubrication problems involving piezo-viscous and couple stress fluid effects.

The comparison between analytical and NNSM solutions illustrates that the developed NNSMs provide highly dependable predictions for pressure, load-carrying capacity, and response time. The extremely small error magnitudes, good regression characteristics, and stable convergence behavior collectively confirm the effectiveness and reliability of the proposed NNSM methodology for modeling nonlinear squeeze film lubrication problems involving complex rheological effects.

The principal novelty of this work lies in combining slip velocity, pressure-dependent viscosity, couple-stress fluid, stochastic surface roughness, and NNSM into a unified analytical and predictive framework for rough circular squeeze film lubrication. Slip velocity and couple-stress fluid enhance lubrication by reducing friction and increasing load capacity, but surface roughness & pressure-dependent viscosity reduce film pressure. The proposed methodology provides an analytical design and optimization tool for journal and thrust bearings, gears, precision machinery, artificial synovial joints, biomedical implants, MEMS, and aerospace lubrication systems.

Future work should extend the proposed model to include thermal effects, cavitation, transient operating conditions, and three-dimensional bearing geometries. Experimental validation and the development of advanced NNSM-based predictive models for real-time lubrication analysis and optimization in engineering applications should also be pursued.

Acknowledgments

The authors would like to thank Nitte (Deemed to be University), NMAM Institute of Technology (NMAMIT), Nitte-574110, Udupi Dist., Karnataka, India.

Funding

None.

Conflict of interest

The authors declare no potential competing interests.

Author contributions

Conceptualization: All authors
Formal analysis: All authors
Investigation: Mallesh Narayanareddy
Methodology: Mallesh Narayanareddy
Writing – original draft: Mallesh Narayanareddy
Writing – review & editing: Vasanth Karegowdar Rajendrappa

Availability of data

Data are available upon reasonable request from the corresponding author.

AI tools statement

All authors confirm that no AI tools were used in the preparation of this manuscript.

References

1. Barus C. Isothermals, isopiestics and isometrics relative to viscosity. *Am J Sci.* 1893;45(266):87-96. https://doi.org/10.2475/ajs.s3-45.266.87
2. Stokes VK. Couple stresses in fluids. *Phys Fluids.* 1966;9(9):1709-1715. https://doi.org/10.1063/1.1761925
3. Bujurke NM, Jayaraman G. The influence of couple stresses in squeeze films. *Int J Mech Sci.* 1982;24(6):369-376. https://doi.org/10.1016/0020-7403(82)90070-4
4. Cameron AGW. *The Principles of Lubrication.* London, UK: Longmans; 1966. Accessed January 1, 1966. https://cir.nii.ac.jp/crid/1970304959943447071
5. Kudenatti RB, Basti DP, Bujurke NM. Numerical solution of the MHD Reynolds equation for squeeze film lubrication between two parallel surfaces. *Appl Math Comput.* 2012;218(18):9372-9382. https://doi.org/10.1016/j.amc.2012.03.019
6. Ramanaiah G. Squeeze films between finite plates lubricated by fluids with couple stress. *Wear.* 1979;54(2):315-320. https://doi.org/10.1016/0043-1648(79)90123-6
7. Elrod HG. A general theory for laminar lubrication with Reynolds roughness. *J Lubr Technol.* 1979;101(1):8-14. https://doi.org/10.1115/1.3453283
8. Tripathi JP, Singh UP, Singh BK. Homotopy analysis of circular plates squeeze film bearings lubricated with couple stress fluids: piezo-viscous model. *Sci Technol J.* 2020;8(2):95-102. https://doi.org/10.22232/stj.2020.08.02.14
9. Hanumagowda BN, Salma A, Raju BT, Nagarajappa CS. The magnetohydrodynamic lubrication of curved circular plates with couple stress fluid. *Int J Pure Appl Math.* 2017;113(6):307-315. Accessed February 13, 2017. https://www.researchgate.net/publication/349589539_The_Magneto-hydrodynamic_Lubrication_of_Curved_Circular_Plates_With_Couple_Stress_Fluid
10. Lin JR, Chu LM, Liang LJ, Lee PH. Derivation of a modified lubrication equation for hydromagnetic non-Newtonian cylindrical squeeze films and its application to circular plates. *J Eng Math.* 2012;77(1):69-75. https://doi.org/10.1007/s10665-012-9540-6
11. Lin JR, Chu LM, Li WL, Lu RF. Combined effects of piezo-viscous dependency and non-Newtonian couple stresses in wide parallel-plate squeeze-film characteristics. *Tribol Int.* 2011;44(12):1598-1602. https://doi.org/10.1016/j.triboint.2011.04.003
12. Lin JR, Chu LM, Liang LJ. Effects of viscosity-pressure dependency on the non-Newtonian squeeze film of parallel circular plates. *Lubr Sci.* 2013;25(1):1-9. https://doi.org/10.1002/ls.1188
13. Hanumagowda BN. Combined effect of pressure-dependent viscosity and couple stress on squeeze-film lubrication between circular step plates. *Proc Inst Mech Eng J J Eng Tribol.* 2015;229(9):1056-1064. https://doi.org/10.1177/1350650115572449
14. Tzeng ST, Saibel E. Surface roughness effect on slider bearing lubrication. *ASLE Trans.* 1967;10(3):334-348. https://doi.org/10.1080/05698196708972191
15. Christensen H. Stochastic models for hydrodynamic lubrication of rough surfaces. *Proc Inst Mech Eng.* 1969;184(1):1013-1026. https://doi.org/10.1243/PIME_PROC_1969_184_074_02
16. Prakash J, Tonder K. Roughness effects in circular squeeze-plates. *ASLE Trans.* 1977;20(3):257-263. https://doi.org/10.1080/05698197708982840
17. Gupta JL, Deheri GM. Effect of roughness on the behaviour of squeeze film in a spherical bearing. *Tribol Trans.* 1996;39(1):99-102. https://doi.org/10.1080/10402009608983508
18. Andharia PI, Gupta JL, Deheri GM. Effect of transverse surface roughness on the behaviour of squeeze film in a spherical bearing. *Appl Mech Eng.* 1999;4(Spec Iss):19-24. Accessed January 9, 1999. http://yadda.icm.edu.pl/baztech/element/bwmeta1.element.baztech-article-BPZ2-0012-0002
19. Andharia PI, Deheri GM, Gupta JL. Effect of longitudinal surface roughness on the behaviour of squeeze film in a spherical bearing. *Int J Appl Mech Eng.* 2001;6(4):885-897. Accessed January 11, 2011. https://www.researchgate.net/publication/255939889_Effect_of_Longitudinal_Surface_Roughness_on_Hydrodynamic_Lubrication_of_Slider_Bearings
20. Naduvinamani NB, Hiremath PS, Gurubasavaraj G. Effect of surface roughness on the couple-stress squeeze film between a sphere and a flat plate. *Tribol Int.* 2005;38(5):451-458. https://doi.org/10.1016/j.triboint.2004.09.001
21. Naduvinamani NB, Apparao S, Hiremath AG. Effect of surface roughness and viscosity-pressure

dependency on the couple stress squeeze film characteristics of parallel circular plates. *Adv Tribol.* 2014;2014:387413.
https://doi.org/10.1155/2014/387413

22. Hanumagowda BN, Raju BT, Santhosh Kumar J, Vasanth KR. Combined effect of surface roughness and pressure-dependent viscosity over couple stress squeeze film lubrication between circular stepped plates. *Proc Inst Mech Eng J J Eng Tribol.* 2018;232(5):525-534.
https://doi.org/10.1177/1350650117721432

23. Fathima ST, Naduvinamani NB, Santhosh Kumar J, Hanumagowda BN. Effect of surface roughness on the squeeze film characteristics of circular plates in the presence of conducting couple stress fluid and transverse magnetic field. *Adv Tribol.* 2015;2015:302396.
https://doi.org/10.1155/2015/302396

24. Hanumagowda BN, Salma A, Nagarajappa CS. Effects of surface roughness, MHD and couple stress on squeeze film characteristics between curved circular plates. *J Phys Conf Ser.* 2018;1000:012075.
https://doi.org/10.1088/1742-6596/1000/1/012075

25. Awati VB, Kengangutti A. Surface roughness effect on thermohydrodynamic analysis of journal bearings lubricated with couple stress fluids. *Nonlinear Eng.* 2019;8(1):397-406.
https://doi.org/10.1515/nleng-2018-0017

26. Byeon H, Latha YL, Hanumagowda BN, et al. Magnetohydrodynamics and viscosity variation in couple stress squeeze film lubrication between rough flat and curved circular plates. *Sci Rep.* 2023;13(1):22960.
https://doi.org/10.1038/s41598-023-50326-7

27. Kalavathi GK, Najar FA, Vasundhara MG. Performance characteristics of journal bearings (porous type): a coupled solution using Hartmann number and roughness parameter. *Proc Inst Mech Eng J J Eng Tribol.* 2020;234(5):668-675.
https://doi.org/10.1177/1350650119886709

28. Hanumagowda BN, Sreekala CK, Kumar V, Kodekalmath VI. An analysis about MHD, couple stress, and the roughness of the surface on a long cylinder and infinite porous plate. In: *Proceedings of the 2022 IEEE 2nd Mysore Sub Section International Conference (MysuruCon).* IEEE; 2022:16-17.
https://doi.org/10.1109/MysuruCon55714.2022.9972468

29. Patel JR, Deheri G. Combined effect of surface roughness and slip velocity on Jenkins model based magnetic squeeze film in curved rough circular plates. *Int J Comput Math.* 2014;2014:367618.
https://doi.org/10.1155/2014/367618

30. Patel JR, Deheri GM. Jenkins model based magnetic squeeze film in curved rough circular plates considering slip velocity: A comparison of shapes. *FME Trans.* 2015;43(2):144-153.
https://doi.org/10.5937/fmet1502144P

31. Sekar S, Nathan SL, Saravanathan LP. Velocity slip with viscosity variation for rough porous circular stepped plates using couple stress fluid. *Math Model Eng Probl.* 2022;9(6):1631-1638.
https://doi.org/10.18280/mmep.090624

32. Dass TD, Gunakala SR, Comissiong DM. Combined effect of variable viscosity and surface roughness on the squeeze film characteristics of infinitely wide rectangular plate with couple stress fluid, velocity-slip and ferrofluid lubricant. *Mater Today Proc.* 2022;56:1717-1725.
https://doi.org/10.1016/j.matpr.2021.10.355

33. Vasanth KR, Mallesh N, Hanumagowda BN, D'Silva SP. A theoretical investigation into the effects of slip velocity and piezo-viscous behaviour on couple stress fluids along circular plates. *Int J Thermofluids.* 2025;27:101176.
https://doi.org/10.1016/j.ijft.2025.101176

34. Mallesh N, Vasanth KR, Hanumagowda BN, D'Silva SP. Analysis of viscosity variation and couple stress fluid based squeezed film lubrication between porous circular plates considering effect of slip velocity. *Surf Rev Lett.* 2026.
https://doi.org/10.1142/S0218625X26500514

35. Ang EHW, Wang G, Ng BF. Physics-informed neural networks for low Reynolds number flows over cylinder. *Energies.* 2023;16(12):4558.
https://doi.org/10.3390/en16124558

36. Chen RTQ, Rubanova Y, Bettencourt J, Duvenaud DK. Neural ordinary differential equations. *arXiv.* 2018.
https://doi.org/10.48550/arXiv.1806.07366

37. Eivazi H, Tahani M, Schlatter P, Vinuesa R. Physics-informed neural networks for solving Reynolds-averaged Navier-Stokes equations. *Phys Fluids.* 2022;34(7):075117.
https://doi.org/10.1063/5.0095270

38. Jin X, Cai S, Li H, Karniadakis GE. NSFnets (Navier-Stokes flow nets): physics-informed neural networks for the incompressible Navier-Stokes equations. *J Comput Phys.* 2021;426:109951.
https://doi.org/10.1016/j.jcp.2020.109951

39. Jafari A. Transport-Embedded Neural Architecture: Redefining the Landscape of Physics-Aware Neural Models in Fluid Mechanics. *arXiv.* 2024.
https://doi.org/10.48550/arXiv.2410.04114

40. Varun Kumar RS, Sowmya G, Prakash C, Chandan K, Prasannakumara BC. Shape factor effect

on the thermal variation of a wavy fin wetted by ternary hybrid nanofluid using an extended physics-informed Laguerre neural network. *Neural Comput Appl.* 2025;37(32):27083-27115. https://doi.org/10.1007/s00521-025-11658-9

41. Chandan K, Karthik K, Nagaraja KV, Prasannakumara BC, Varun Kumar RS, Muhammad T. Radiative heat transfer analysis of a concave porous fin under the local thermal non-equilibrium condition: application of the clique polynomial method and physics-informed neural networks. *Appl Math Mech.* 2024;45(9):1613-1632. https://doi.org/10.1007/s10483-024-3143-6

42. Sanju BS, Naveen Kumar R, Varun Kumar RS, Abdulrahman A. Physics-informed neural network approach to analyze the onset of oscillatory and stationary convections in chemically triggered Navier-Stokes-Voigt fluid layer heated and salted from below. *Appl Math Mech.* 2025;46(11):2199-2220. https://doi.org/10.1007/s10483-025-3316-7

43. Chandan K, Varun Kumar RS, Sharma N, et al. Advanced deep learning approach with physics-informed neural networks for analysing the thermal variation through a radial fin applicable in heat exchangers. *Pramana.* 2024;98(3):123. https://doi.org/10.1007/s12043-024-02823-1

44. Varun Kumar RS, Chandan K, Venkadeshwaran K, Muhammad T, Punith Gowda RJ, Prasannakumara BC. Influence of magnetic dipole on the hybrid nanofluid flow with chemical reactions due to the generated and absorbed heat. *Pramana.* 2025;99(2):65. https://doi.org/10.1007/s12043-025-02917-4

45. Varun Kumar RS, Abhilasha SK, Raghunandan ME, Abdulrahman A, Naveen Kumar R. Comprehensive analysis on the thermal performance of circular-perforated rectangular fin with internal heat generation using Chelyshkov polynomial operational matrix-based collocation approach. *Int J Mech Mater Des.* 2025;21(6):2105-2128. https://doi.org/10.1007/s10999-025-09815-y

46. Shah K, Abdeljawad T, Abdalla B, Ali Z. Analyzing a coupled dynamical system of materials recycling in chemostat systems with artificial deep neural network. *Model Earth Syst Environ.* 2025;11(5):313. https://doi.org/10.1007/s40808-025-02473-1

47. Shah K, Khan A, Abdeljawad T, Eiman T. Using deep neural network and fractional derivative to investigate evolution of virulence. *Contemp Math.* 2026;7(2):1386-1415. https://doi.org/10.37256/cm.7220269398

48. Shah K, Sarwar M, Abdeljawad T. Study of fractional order epidemic compartmental model by using artificial deep neural networks. *Neural Netw.* 2025;192:107944. https://doi.org/10.1016/j.neunet.2025.107944

Mallesh Narayanareddy *received his B.Sc. degree from Vidya Vahini First Grade College, Tumkur, India. He received his M.Sc. degree from Tumkur University, India. He is currently working as an assistant professor in the Department of Mathematics at Sahyadri College of Engineering & Management, Mangalore. His research interests are tribology and Graph theory.*
https://orcid.org/0009-0002-6833-5264

Vasanth Karegowdar Rajendrappa *received his B.Sc. degree from Mangalore University, Mangalore, India. He received his M.Sc. degree from Manipal Academy of Higher Education, Manipal, India. He received his Ph.D. from REVA University, Bangalore, India. He is currently working as an Associate Professor & Head in the Department of Mathematics, NMAMIT, Nitte, Udupi, India. His research interests are tribology and Partial differential equations.*
https://orcid.org/0000-0002-4142-9423

An International Journal of Optimization and Control: Theories & Applications (https://accscience.com/journal/ijocta)